

# Limitations of Data-Driven Spectral Reconstruction – Optics-Aware Analysis and Mitigation

QIANG FU\* and MATHEUS SOUZA\*, KAUST, Saudi Arabia

EUNSUE CHOI, SUHYUN SHIN, and SEUNG-HWAN BAEK, POSTECH, Korea

WOLFGANG HEIDRICH, KAUST, Saudi Arabia

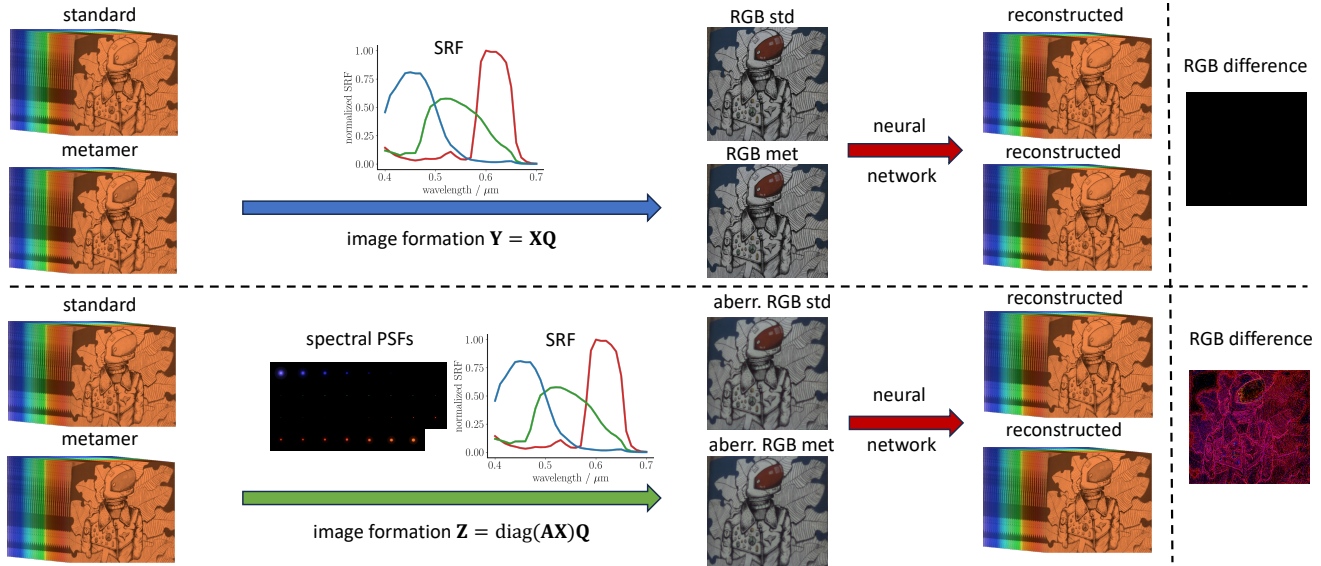


Fig. 1. Spectral image formation models used in the analysis in this work. Top: In the NTIRE spectral recovery challenges, an RGB image is considered as a linear projection from a high-dimensional hyperspectral datacube to a 3D color image. The existence of metamerism results in identical RGB images for different spectra. The neural network trained in this way cannot distinguish their corresponding spectra. Bottom: A possible mitigation to this problem is to include the optical aberrations of the lens in the image formation model. Spectral information is encoded into the aberrated RGB images, enabling the neural network to tell the difference between metamers. In both cases, the RGB image differences are shown on the right (intensity enhanced for better visualization).

Hyperspectral imaging empowers machine vision systems with the distinct capability of identifying materials through recording their spectral signatures. Recent efforts in data-driven spectral reconstruction aim at extracting spectral information from RGB images captured by cost-effective RGB cameras, instead of dedicated hardware.

In this paper we systematically analyze the performance of such methods, evaluating both the practical limitations with respect to current datasets and overfitting, as well as fundamental limitations with respect to the nature

of the information encoded in the RGB images, and the dependency of this information on the optical system of the camera.

We find that, the current models are not robust under slight variations, *e.g.*, in noise level or compression of the RGB file. Without modeling under-represented spectral content, existing datasets and the models trained on them are limited in their ability to cope with challenging metameric colors. To mitigate this issue, we propose to exploit the combination of metameric data augmentation and optical lens aberrations to improve the encoding of the metameric information into the RGB image, which paves the road towards higher performing spectral imaging and reconstruction approaches.

Additional Key Words and Phrases: Hyperspectral imaging, Spectral reconstruction from RGB, Metamerism, Overfitting, Aberration.

## 1 INTRODUCTION

(Hyper)spectral imaging is a method that involves recording the light in a scene in the form of many, relatively narrow, spectral bands, rather than projected into three broadband RGB color channels. Where RGB imaging utilizes the trichromaticity theory of human color vision, spectral imaging provides additional information that can help discriminate between different materials and lighting conditions that are hard to tell apart in RGB images. For example, red stains in a crime scene could be blood, or paint, or a dyed cloth,

\*Both authors contributed equally to this research.

Authors' addresses: Qiang Fu, qiang.fu@kaust.edu.sa; Matheus Souza, matheus.medeirosdesouza@kaust.edu.sa, KAUST, Thuwal, Saudi Arabia, 23955-6900; Eunsue Choi, ches7283@postech.ac.kr; Suhyun Shin, shshin9812@postech.ac.kr; Seung-Hwan Baek, shwbaek@postech.ac.kr, POSTECH, Pohang, Korea, 37673; Wolfgang Heidrich, KAUST, Thuwal, Saudi Arabia, wolfgang.heidrich@kaust.edu.sa.

Permission to make digital or hard copies of all or part of this work for personal or classroom use is granted without fee provided that copies are not made or distributed for profit or commercial advantage and that copies bear this notice and the full citation on the first page. Copyrights for components of this work owned by others than the author(s) must be honored. Abstracting with credit is permitted. To copy otherwise, or republish, to post on servers or to redistribute to lists, requires prior specific permission and/or a fee. Request permissions from permissions@acm.org.

© 2024 Copyright held by the owner/author(s). Publication rights licensed to ACM. ACM XXXX-XXXX/2024/4-ART <https://doi.org/10.1145/nnnnnnnn.nnnnnnnn>

which cannot be distinguished from their RGB colors. Skin tumors could not be diagnosed from surrounding tissues of the same color. It is difficult to spot and sort out plastic leaves from living plants by their greenish colors. Therefore, spectral imaging has been applied in many fields, including computer graphics [Kim 2013], machine vision [Fauvel et al. 2012; Rangnekar et al. 2022], healthcare [Lu and Fei 2014], agriculture [Dale et al. 2013], and environment [Banerjee et al. 2020], to name just a few.

However, conventional hyperspectral cameras require scanning mechanisms [Huang et al. 2022; Lodhi et al. 2019] to acquire the 3D hyperspectral datacube with 2D sensors. To simplify the demanding hardware, extensive efforts have been made in the development of various snapshot hyperspectral cameras [Jeon et al. 2019; Saragadam and Sankaranarayanan 2019; Wagadarikar et al. 2008].

On the extreme end of these hardware simplification efforts, deep learning methods have emerged in recent years that attempt to solve the problem entirely in software by reconstructing spectral data from RGB images. This has resulted in three CVPR-hosted NTIRE challenges [Arad et al. 2018, 2020, 2022] and various network architectures [Cai et al. 2022b; Li et al. 2020; Shi et al. 2018; Zhang et al. 2022; Zhao et al. 2020]. Yet it remains unclear how these methods generalize to unseen data, how they deal with the difficult but important problem of resolving metamerism [Hill 1999; Ortega et al. 2020], and how they depend on the optical system of both the RGB source and the spectral cameras used to capture the datasets.

At its core, estimating spectral information from RGB colors is an ill-conditioned one-to-many mapping problem. As stated by Pharr et al. [Pharr et al. 2023] (Ch. 4), “any such conversion is inherently ambiguous due to the existence of metamers”. Intuition would therefore suggest that the achievable spectral fidelity of RGB to spectral methods is limited. However, this intuition flies in the face of very high numerical test results reported in recent NTIRE challenges [Arad et al. 2018, 2020, 2022].

One possible explanation for the experimental success of spectral reconstruction from an RGB image is that the networks learn to exploit spatial structure to reconstruct spectral information. However, in practice metameric or near-metameric colors often occur in situations where the spatial structure is also similar, e.g. vein finding (the global geometry is a segment of a forearm, but vein structure is unknown), or biometrics (e.g., distinguishing real faces from masks or images). To illustrate this effect, we show an example from the smaller and older CAVE dataset [Yasuma et al. 2010] `fake_and_real_food_ms`, where several fake and real objects are presented in two groups, as shown in Fig. 2. Two sample points from the two red peppers (one real and the other fake, but it’s unclear which is which) have the RGB values [86, 21, 10] and [86, 21, 8], respectively. As can be seen, the real spectra of the real and fake red peppers differ substantially in the red part of the spectrum. A pre-trained model (arbitrarily chosen from previous NTIRE challenges trained on the much larger and newer ARAD1K dataset [Arad et al. 2022]) predicts spectra that differ from the ground truth, but more importantly, the predicted spectra for the real and fake pepper are almost identical, illustrating the failure to adequately deal with metamers.

In this paper, we take a systematic and outside-the-box look at all the above aspects. To the best of our knowledge, we are the first

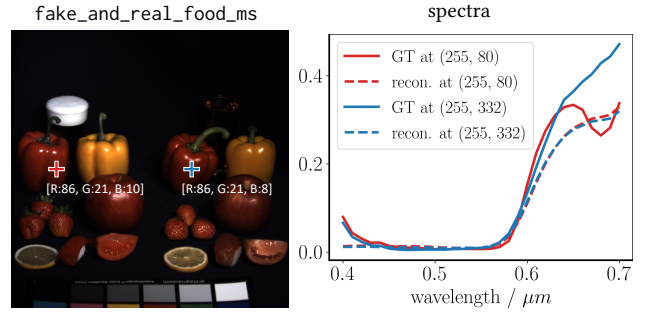


Fig. 2. An example scene `fake_and_real_food_ms` from the CAVE dataset [Yasuma et al. 2010] consists of objects with visually similar colors, but actually different spectra. Left: Color image with highlighted points on the red peppers. Their RGB values are nearly the same. Right: Ground-truth and reconstructed spectra at the corresponding points show their spectral differences. The reconstructed spectra are predicted by the pre-trained MST++ model [Cai et al. 2022b] on the ARAD1K dataset [Arad et al. 2022]. The neural network struggles to distinguish either the two spectra from each other, or from their true spectra.

to analyze, document, and discuss the inherent shortcomings of this research theme. We highlight realistic conditions under which recent efforts fall short, aiming to constructively instigate, debate, provide insights, and forge a new path regarding the physical phenomena that have been overlooked. By conducting a series of adversarial attacks and thorough analysis, we reveal a number of shortcomings in both current datasets and reconstruction methods. Specifically, we find that:

- Existing hyperspectral image datasets severely lack in diversity especially with respect to metameric colors but also other factors including nuisance parameters such as noise and compression ratios.
- State-of-the-art methods suffer from *atypical* overfitting problems that arise from various factors in the image simulation pipeline, such as noise, RGB data format, and lack of optical aberrations.
- Optical aberrations in RGB images, while currently ignored by all methods, are actually *beneficial* rather than harmful to spectral reconstruction *if modeled accurately*.
- Crucially, the limitations of the datasets that we document not only affect the RGB to spectral work, but also any other spectral reconstruction and processing that uses the same training data [Arguello et al. 2021; Jacome et al. 2023; Xu et al. 2024]. We show how *metameric augmentation* can be used to at least partially overcome the dataset issues.

Through the evidence in this work, we contribute to a deepened understanding of the limitations of current datasets as well as of underlying sources that result in the limitations of spectral reconstruction accuracy. The results of the interplay between metameric spectra and optical aberrations opens the door for new approaches for spectral recovery down the road.

## 2 RELATED WORK

### 2.1 Hyperspectral cameras

Conventional hyperspectral imaging systems require filter wheels, liquid-crystal tunable filters, or mechanical motion (e.g., pushbroom) [Huang et al. 2022; Lodhi et al. 2019] to scan the 3D hyperspectral datacube. To enable snapshot acquisition, coded-aperture snapshot spectral imager (CASSI) [Choi et al. 2017b; Wagadarikar et al. 2008] has been proposed to achieve high spectral accuracy using spectrum-dependent coded patterns. Recent methods also exploit spectrally encoded point spread functions (PSFs) to computationally reconstruct a hyperspectral image [Baek et al. 2017; Cao et al. 2011; Jeon et al. 2019]. In general, great efforts have been made to simplify hyperspectral camera hardware by software reconstruction.

### 2.2 Spectral reconstruction from RGB images

A recent trend to solve the snapshot hyperspectral imaging problem is to exploit hyperspectral data with deep neural networks to reconstruct spectral information from RGB images [Arad and Ben-Shahar 2016]. Owing to the wide availability of RGB cameras, this approach seems to be a promising candidate for hyperspectral imaging if successful. A large number of neural network architectures have been proposed in the past three NTIRE spectral recovery challenges [Arad et al. 2018, 2020, 2022]. Our analysis in this paper focuses on this class of methods to gain insights on their strengths and limitations.

### 2.3 Dataset bias and data augmentation

Deep neural networks are prone to suffer from data bias [Fabrizzi et al. 2022; Torralba and Efros 2011] and overfitting problems [Bejani and Ghatee 2021]. Overfitting can lead to the inability of trained models to generalize in real-world applications [Kornblith et al. 2019]. Although overfitting can sometimes be detected by inspecting the training and validation performance over the course of training, it can often be imperceptible in challenging problems. A useful technique to detect overfitting is to use adversarial examples [Werpachowski et al. 2019] generated from the original dataset. On the other hand, it is important to address overfitting when the amount of data is limited. Data augmentation [Rebuffi et al. 2021; Shorten and Khoshgoftaar 2019] techniques are usually employed to improve the robustness of deep neural networks.

### 2.4 Metamerism

Metamerism is a physical phenomenon where distinct spectra produce the same color [Akbarinia and Gegenfurtner 2018] as the high-dimensional spectral space is projected down to three dimensions of a trichromatic vision system (either the human eye or an RGB camera). This phenomenon has been studied in color science [Foster et al. 2006; Thornton 1998], spectral rendering [Jakob and Hanika 2019; Van De Ruit and Eisemann 2023; Weidlich et al. 2021], and hyperspectral imaging [Foster and Amano 2019; Hill 1999]. In hyperspectral imaging [Cukierski and Foran 2010; Ortega et al. 2020], it is crucial for many applications to distinguish between metamers or near-metamers (i.e., different spectra that project to *similar* RGB values). Indeed spectral imaging is usually employed when the RGB

color differences between two materials or features are too small to reliably distinguish between them. Therefore, hyperspectral imaging systems require special attention in the system design to acquire accurate spectral signatures [Hill 2002; Ji et al. 2023].

## 3 FUNDAMENTALS

### 3.1 Spectral image formation

We denote the hyperspectral image as a matrix  $\mathbf{X} \in \mathbb{R}^{MN \times K}$ , where  $M, N$  are the number of pixels, and  $K$  is the number of spectral bands. Note that we have stacked the 2D spatial dimensions in rows of  $\mathbf{X}$ . The spectral response function (SRF) of the camera can be expressed as a matrix  $\mathbf{Q} \in \mathbb{R}^{K \times 3}$ . Therefore, the spectrum-to-color projection results in a color image

$$\mathbf{Y} = \mathbf{X}\mathbf{Q}, \quad (1)$$

where  $\mathbf{Y} \in \mathbb{R}^{MN \times 3}$ . This is the color formation model in the NTIRE 2022 challenge [Arad et al. 2022]. The inverse problem is to recover  $\mathbf{X}$  from  $\mathbf{Y}$ .

In the past NTIRE challenges [Arad et al. 2018, 2020, 2022], optical aberrations haven't been included in the image simulation pipeline. However, the optical system of the RGB camera inevitably introduces spectrally-varying blurs to the spectral images, which is modeled as PSFs. This optical process can be described by a linear matrix-vector product in each spectral band followed by a sum over the spectral dimension. The spectral images through the optical system are  $\mathbf{W} = \text{diag}(\mathbf{A}\mathbf{X})$ , where  $\mathbf{A} \in \mathbb{R}^{KMN \times MN}$  is a block matrix that stacks the spectral PSF matrices vertically, and  $\text{diag}(\cdot)$  extracts the diagonal blocks. The final RGB image is then

$$\mathbf{Z} = \text{diag}(\mathbf{A}\mathbf{X})\mathbf{Q}, \quad (2)$$

where  $\mathbf{Z} \in \mathbb{R}^{MN \times 3}$ . With the optical image formation model accounted for, the inverse problem is to recover  $\mathbf{X}$  from  $\mathbf{Z}$ . See Appendix for the detailed image formation models.

The two spectral image formation models are illustrated in Fig. 1. Without considering optical aberrations (Eq. (1)), the neural network struggles to reconstruct the real hyperspectral images in the presence of metamers. The spectrally-varying PSFs (Eq. (2)) are helpful to mitigate this issue since the aberrated RGB images from metamers are different. In the following sections, we will discuss the limitations of existing data-driven spectral reconstruction based on these two image formation models in detail.

### 3.2 Hyperspectral datasets and data diversity

Compared to very large color (RGB) image datasets (e.g., ImageNet [Deng et al. 2009], DIV2K [Agustsson and Timofte 2017]), hyperspectral datasets are far smaller in size, primarily limited by the unavailability of high-quality hyperspectral cameras and the difficulty in acquiring outside the lab with moving target scenes. The largest dataset so far is ARAD1K used in the NTIRE 2022 challenge [Arad et al. 2022]. In addition, we also include the CAVE [Yasuma et al. 2010], ICVL [Arad and Ben-Shahar 2016], and KAUST [Li et al. 2021] datasets that share the same spectral range to extend our experiments. The datasets are summarized in Table 1. Although other datasets [Chakrabarti and Zickler 2011; Choi et al. 2017a; Monno et al. 2015] exist, they cover slightly different spectral bands, making

direct comparisons difficult. We therefore restrict our analysis to the datasets listed in the table.

The difficulties in the data capture not only affect the size but also the *diversity* of the datasets. In particular, effects like metamerism, which are comparatively rare in everyday environments [Foster et al. 2006; Prasad and Wenhe 2015], yet crucial for many actual applications of spectral imaging, are under-represented in the datasets. While the CAVE dataset [Yasuma et al. 2010] contains some fake-and-real pairs of objects (e.g., Fig. 2) to account for metamerism, the total amount of such data is still very low. We analyze the general data diversity issue in Section 4 and the specific case of metamerism in Section 5.

### 3.3 Modeling metamerism

Since there are not enough examples of metamerism in existing datasets, their effects in spectral reconstruction went unnoticed in prior works. On the one hand, we need adversarial examples to reveal the unexplored problems. On the other hand, we want to investigate how they can complement the current datasets. Therefore, we propose a new form of data augmentation in our experiments. *Metameric augmentation* starts with existing spectral images and creates a new, *different* spectral image that however maps to the same RGB image (given a specific set of RGB spectral response functions). In Section 5, we first use metameric augmentation as an adversarial example to reveal the previously omitted effects of metamerism on the performance discrepancy. In Section 6, we show metameric augmentation is beneficial to mitigate the raised problems along with an aberration-aware training strategy.

Note that data augmentation has proven to be effective in deep learning to mitigate data shortage. Color image augmentation techniques have been focusing mainly on geometric transformations and intensity adjustment. Although these techniques have been employed in prior methods, they only augment the spatial dimensions in hyperspectral images. To the best of our knowledge, metameric augmentation beyond RGB colors, accounting for the physical phenomenon of metamerism, has not been adopted before in spectral reconstruction problems. Metameric augmentation can greatly enrich the **spectral content** in existing datasets to mitigate the lack of diversity.

Interestingly, metamer generation from existing spectra has been studied in color science and spectral rendering to accurately model the scenes using various methods, e.g., metameric black [Alsam and Lenz 2007; Finlayson and Morovic 2005; van Trigt 1994] and spectral uplifting [Belcour et al. 2023; Jakob and Hanika 2019; Van De Ruit and Eisemann 2023]. In this work, to support our analysis, we adopt the metameric black approach to generate metamers, whereas we note that other metamer generation methods can also be employed for the same purpose.

A spectrum  $\mathbf{S}$  can be projected onto two orthogonal subspaces, one for the fundamental metamer  $\mathbf{S}^*$ , and the other for metameric black  $\mathbf{B}$  [Cohen and Kappauf 1982; Viénot and Brettel 2014]. A new metameric spectrum  $\mathbf{S}'$  is then

$$\mathbf{S}' = \mathbf{S}^* + \alpha \mathbf{B}, \quad (3)$$

where  $\mathbf{S}^* = \mathbf{Q} \left( \mathbf{Q}^T \mathbf{Q} \right)^{-1} \mathbf{Q}^T \mathbf{S}$  and  $\mathbf{B} = \mathbf{S} - \mathbf{S}^*$ . Since adding metameric black does not alter the RGB color, we can vary the coefficient  $\alpha$  to generate different spectra that are all metamers. To avoid negative spectral radiance, we clip the negative values in the generated spectra and re-calculate the RGB colors for the affected pixels. See Appendix for the analysis on the effects of clipping to non-negative values while generating metamer data.

### 3.4 Performance evaluation metrics

Consider a hyperspectral image  $\mathbf{X}_{k,i,j}$  and its estimate  $\hat{\mathbf{X}}_{k,i,j}$ , where  $k$  is the spectral index, and  $i, j$  are spatial indices. The reconstruction quality can be evaluated in various ways. The NTIRE 2022 spectral reconstruction challenge [Arad et al. 2022] adopts two numerical metrics, Mean Relative Absolute Error (MRAE),

$$\text{MRAE} = \frac{1}{KMN} \sum_{k,i,j} |\hat{\mathbf{X}}_{k,i,j} - \mathbf{X}_{k,i,j}| / \mathbf{X}_{k,i,j}, \quad (4)$$

$$(5)$$

and Root Mean Square Error (RMSE)

$$\text{RMSE} = \sqrt{\frac{1}{KMN} \sum_{k,i,j} \left( \hat{\mathbf{X}}_{k,i,j} - \mathbf{X}_{k,i,j} \right)^2}. \quad (6)$$

Another metric widely used in hyperspectral imaging is the Spectral Angle Mapper (SAM) [Kuching 2007; Park et al. 2007; Van der Meer 2006], although it has not yet found its way into the relevant computer vision literature. SAM emphasizes the spectral accuracy compared to the previous metrics, which are more forgiving of large errors in individual spectral channels:

$$\text{SAM} = \frac{1}{MN} \sum_{i,j} \cos^{-1} \left( \frac{\sum_k \hat{\mathbf{X}}_{k,i,j} \mathbf{X}_{k,i,j}}{\sqrt{\sum_k \hat{\mathbf{X}}_{k,i,j}^2 \sum_k \mathbf{X}_{k,i,j}^2}} \right). \quad (7)$$

Finally, we also inspect the spatial quality in individual spectral channels, and calculate the spectrally averaged Peak Signal-to-Noise Ratio (PSNR),

$$\text{PSNR} = \frac{1}{K} \sum_k 20 \log_{10} \left( \frac{\text{MAX}}{\sqrt{\text{MSE}_k}} \right), \quad (8)$$

where MAX is the maximum possible value, and  $\text{MSE}_k$  is the mean squared error in the  $k$ -th spectral band. This metric complements RMSE to account for performance variation in individual spectral bands.

### 3.5 Training details

In our study, we conduct all the experiments across various datasets and network architectures. Following the methodologies proposed by the latest champion network MST++ [Cai et al. 2022b], we employ their patch-wise training approach (patches of 128×128 pixels).

**3.5.1 Data Preparation.** Throughout the experiments in this work, we follow the same data format (Matlab-compatible mat files) for hyperspectral images in the ARAD1K dataset [Arad et al. 2022]. To be consistent, we also convert the raw hyperspectral datacubes in the CAVE [Yasuma et al. 2010], ICVL [Arad and Ben-Shahar 2016], and KAUST [Li et al. 2021] datasets to this format. The data values

Table 1. Basic information of four existing hyperspectral datasets.

Dataset	Spectra (nm)	Resolution (x, y, $\lambda$ )	Amount	Device	Scene
CAVE [Yasuma et al. 2010]	400:10:700	$512 \times 512 \times 31$	32	monochrome sensor + tunable filters	lab setup
ICVL [Arad and Ben-Shahar 2016]	400:10:700	$1392 \times 1300 \times 31$	201	HS camera (Specim PS Kappa DX4)	outdoor
KAUST [Li et al. 2021]	400:10:700	$512 \times 512 \times 31$	409	HS camera (Specim IQ)	outdoor
ARAD1K [Arad et al. 2022]	400:10:700	$482 \times 512 \times 31$	1000	HS camera (Specim IQ)	outdoor

are normalized by their respective bit-depths such that the data range is  $[0.0, 1.0]$ . The training and validation sets in ARAD1K are kept the same as offered in the NTIRE 2022 spectral recovery challenge [Arad et al. 2022], *i.e.*, 900 files for training, and 50 for validation. We split the CAVE, ICVL, and KAUST datasets by 90% for training, and 10% for validation. Following the training strategy in MST++ [Cai et al. 2022b], we keep the training and validation lists fixed.

**3.5.2 Metamer Generation.** We adopt the metameric black method [Alsam and Lenz 2007; Finlayson and Morovic 2005; van Trigt 1994] to generate metamers from the original hyperspectral data. By varying the coefficient of the metameric black term, we could generate metamers that project to the same RGB color. Note that the original datacube corresponds to  $\alpha = 1$ , and the fundamental metamer corresponds to  $\alpha = 0$ . For the experiments with fixed metamers, we use the fundamental metamers to complement the original standard data. This is sufficient to demonstrate our findings. Other arbitrary values would result in the same conclusions. A more aggressive setting is to vary  $\alpha$  as a variable to account for the infinite possible metamers in a more realistic situation.

**3.5.3 Training and Validation Procedure.** Following the training strategies in MST++ [Cai et al. 2022b], we sub-sample the hyperspectral datacubes and the corresponding RGB images into overlapping patches of  $128 \times 128$ . Spatial augmentations, such as random rotation, vertical flipping, and horizontal flipping are randomly applied to the training patches. In the validation step, we calculate the evaluation metrics (MRAE, RMSE, PSNR, and SAM) on the full spatial resolution for the ARAD1K ( $482 \times 512$ ), CAVE ( $512 \times 512$ ), and KAUST ( $512 \times 512$ ) datasets. Note that this is different from MST++ [Cai et al. 2022b] where only the central  $256 \times 256$  regions are evaluated. The ICVL dataset has a very large spatial resolution ( $1300 \times 1392$ ). To be consistent with other datasets, we evaluate ICVL only in the central  $512 \times 512$  regions.

Similar as MST++, in each epoch, we train the networks for 1000 iterations, with a total number of 300 epochs. All the reported results are evaluated at the end of the training epochs, *i.e.*, 300k iterations. We find that the training iterations are sufficient to achieve convergence in all our proposed experiments. Hyperparameters, such as learning rate and batch size, are tuned to achieve the best performance for each network on each dataset.

All the experiments are conducted on an NVIDIA A100 GPU (80 GB memory).

## 4 FINDING 1: ATYPICAL OVERFITTING

Although it is well-known that deep neural networks may suffer from overfitting problems, we find that the overfitting behavior

in spectral reconstruction is atypical and difficult to notice with standard evaluations. Here we introduce minimalist changes to the ARAD1K dataset used in NTIRE 2022 challenge [Arad et al. 2022] in three experiments to demonstrate it. We evaluate 11 top-performant neural network architectures, namely MST++ [Cai et al. 2022b], MST-L [Cai et al. 2022a], MPRNet [Zamir et al. 2021], Restormer [Zamir et al. 2022], MIRNet [Zamir et al. 2020], HINet [Chen et al. 2021], HDNet [Hu et al. 2022], AWAN [Li et al. 2020], EDSR [Lim et al. 2017], HRNet [Zhao et al. 2020], and HSCNN+ [Shi et al. 2018].

### 4.1 Training with less data

First, we make a simple change to the training of the participating networks in the NTIRE 2022 challenge [Arad et al. 2022]. While keeping all the training settings intact, we randomly choose only 50% or 20% of the original training data, respectively, to train the candidate networks and validate the performance on the original validation data. We illustrate the validation curves for MST++ [Cai et al. 2022b] in Fig. 3. See the Supplemental Material for the results of other networks. We summarize the results for 100% and 50% training data in Table 2 for all networks.

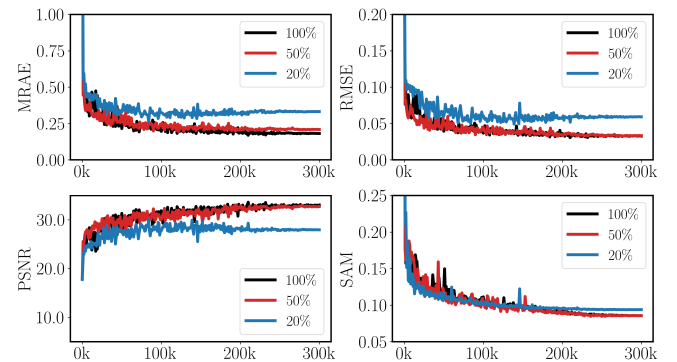


Fig. 3. Validation performance for MST++ [Cai et al. 2022b] with 100%, 50%, and 20% of the original training data on ARAD1K [Arad et al. 2022].

Although the performance with less training data deviates mildly in MRAE, RMSE, and PSNR, the spectral accuracy SAM (highlighted in bold in Table 2) is surprisingly less affected. In particular, some networks (*e.g.*, MST++ [Cai et al. 2022b], MIRNet [Zamir et al. 2020]) achieve exactly the same SAM scores. MST-L [Cai et al. 2022a] (50%) even improves SAM slightly, placing itself the best among all.

We therefore paradoxically find that despite the small size of hyperspectral datasets, the data already seems to be redundant. This serves as a first indication that the *diversity* of the datasets

Table 2. Performance comparison with 100% and 50% of training data for different methods on the original ARAD1K dataset.

Network	Data	MRAE↓	RMSE↓	PSNR↑	SAM↓
MST++	100%	0.182	0.033	33.0	<b>0.086</b>
	50%	0.209	0.033	32.7	<b>0.086</b>
MST-L	100%	0.184	0.031	33.5	<b>0.084</b>
	50%	0.253	0.042	30.6	<b>0.080</b>
MPRNet	100%	0.212	0.034	32.5	<b>0.084</b>
	50%	0.293	0.039	31.3	<b>0.091</b>
Restormer	100%	0.204	0.033	33.2	<b>0.083</b>
	50%	0.304	0.041	31.4	<b>0.092</b>
MIRNet	100%	0.186	0.030	33.7	<b>0.082</b>
	50%	0.214	0.033	32.6	<b>0.082</b>
HINet	100%	0.234	0.036	32.3	<b>0.085</b>
	50%	0.267	0.041	30.7	<b>0.090</b>
HDNet	100%	0.223	0.038	31.2	<b>0.095</b>
	50%	0.296	0.047	28.9	<b>0.097</b>
AWAN	100%	0.213	0.034	32.2	<b>0.091</b>
	50%	0.273	0.042	30.5	<b>0.095</b>
EDSR	100%	0.358	0.052	27.3	<b>0.095</b>
	50%	0.430	0.059	26.1	<b>0.093</b>
HRNet	100%	0.388	0.057	26.4	<b>0.094</b>
	50%	0.413	0.065	25.5	<b>0.096</b>
HSCNN+	100%	0.428	0.066	25.4	<b>0.098</b>
	50%	0.462	0.068	25.0	<b>0.101</b>

is severely lacking. We analyze this effect in more depth in the following experiments.

## 4.2 Validation with unseen data

To further scrutinize the underlying issue, we validate existing pre-trained models with “unseen” data synthesized from the original dataset used in the NTIRE challenge. The challenge organizers state that “the exact noise parameters and JPEG compression level used to generate RGB images for the challenge was kept confidential” [Arad et al. 2022]. Only the spectrum-to-color projection was considered, and no aberrations of the optical system were simulated.

In our experiments, we generate new RGB images using the same methodology and calibration data, but different noise and compression settings. Specifically, we use the SRF data for a Basler ace 2 camera (model A2a5320-23ucBAS) known to the networks, and simulate Poisson noise at varying noise levels by controlling the number of photon electrons (npe). We adopt the same rudimentary in-camera image signal processing pipeline. As an illustrative example, we use MST++ [Cai et al. 2022b] in Table 3, Row 1 as a reference for comparison; results for other networks can be found in the Supplemental Material.

First, as a baseline, we consider a noiseless (npe = 0) and aberration-free case with moderate JPEG compression quality (Q = 65), shown in Table 3, Row 2. The results show significant drops in all the performance metrics. Note that the only differences here compared to the challenge dataset are the noise level and compression quality – the base images are identical! This indicates that the network overfits both the noise and JPEG compression parameters.

Second, in Row 3, we generate noiseless RGB images, but in lossless PNG format, as opposed to the JPEG (Q = 65) in Row 2. Note that JPEG compression is not necessary for the core inverse problem in hyperspectral imaging, since raw data could be readily obtained from the sensors. This results in paradoxical reconstruction performance. MRAE and SAM improve compared to Row 2 (but are still worse than Row 1), while RMSE and PSNR deteriorate further. Considering this only eliminates image compression, and the networks were trained on MRAE [Cai et al. 2022b], we can confirm that the network indeed overfits the specific unknown JPEG compression used in the challenge [Arad et al. 2022].

Third, we consider a more realistic imaging scenario, in which we eliminate the impact of unnecessary compression by employing the lossless PNG format to save the RGB images (equivalent to using raw camera data). We adopt moderate noise levels (npe = 1000) and realistic optical aberrations from a recent double Gauss lens patent [Ichimura 2021] to mimic a real photographic camera. We can observe a further performance drop in Row 4, which provides additional evidence that the network overfits the unknown parameters in the image simulation pipeline [Arad et al. 2022]. When used under realistic imaging conditions, the performance degrades significantly.

## 4.3 Cross-dataset validation

In addition, we inspect the effects of different datasets (*cf.* Table 1) on the performance. We train the MST++ network on the four datasets with the same image simulation parameters. To eliminate the impact of other factors, we choose the ideal noiseless and aberration-free condition without compression. In the validation, we use our trained model on ARAD1K dataset to validate on the other three datasets, respectively. In Table 4, we compare the performance with the models both trained and validated on the original datasets. Results for other networks can be found in the Supplement. They all illustrate the same difficulties in generalization.

Even though the imaging conditions are the same and ideal, the network trained on one dataset experiences significant performance drop in all metrics when validated on other datasets. This indicates that the contents of the datasets, as well as the acquisition devices used to capture the datasets, play important roles.

We also point out that the CAVE dataset [Yasuma et al. 2010], although smaller and older than the others, is more difficult to train for better performance. This is probably due to the fact that CAVE consists of several challenging scenes of real and fake objects that appear in similar colors, but other datasets comprise less aggressive natural scenes.

## 4.4 Discussion

The experiments conducted in this section clearly highlight several shortcomings with respect to the existing datasets: **(1) they lack diversity in nuisance parameters** such as noise and compression ratios, and **(2) they lack scene diversity**. While we show in this document the results for the largest available dataset (ARAD1K), the Supplement shows consistent results for all the datasets. Both of these aspects result in over-fitting and prevent the networks from learning the general spectral image restoration task. Next we

Table 3. Evaluation of the pre-trained MST++ model on synthesized validation data from the ARAD1K dataset with different noise levels, compression quality, and realistic optical aberrations.

	Data property				MRAE ↓	RMSE ↓	PSNR ↑	SAM ↓
	Data source	Noise (npe)	RGB format	Aberration				
1	NTIRE 2022	unknown	jpg (Q unknown)	None	0.170	0.029	33.8	0.084
2	Synthesized	0	jpg (Q = 65)	None	0.460	0.049	29.2	0.094
3		0	png (lossless)	None	0.362	0.057	28.7	0.087
4		1000	png (lossless)	CA*	0.312	0.055	28.4	0.118

\*CA: chromatic aberration, from a patent double Gauss lens (US20210263286A1).

Table 4. Cross-dataset validation example using MST++ [Cai et al. 2022b].

Trained on	Validated on	MRAE↓	RMSE↓	PSNR↑	SAM↓
CAVE	CAVE	0.237	0.034	31.9	0.194
ARAD1K	CAVE	1.626	0.074	24.4	0.376
ICVL	ICVL	0.079	0.019	38.3	0.024
ARAD1K	ICVL	0.627	0.091	22.0	0.110
KAUST	KAUST	0.069	0.013	44.4	0.061
ARAD1K	KAUST	1.042	0.100	22.0	0.370

specifically analyze the effect of metamerism; the analysis of the impact of optical aberrations will be deepened in Section 6.

## 5 FINDING 2: METAMERIC FAILURE

In this section, we inspect the performance of existing methods using metamer as an adversary to validate as well as re-train the neural networks for performance analysis.

### 5.1 Validation with metamers

We generate metamer datacubes (metamer data) from the original ARAD1K dataset (standard data) using the metameric black method [Finlayson and Morovic 2005]. For this set of experiments, we fix the coefficient  $\alpha = 0$  in Eq. (3). We choose a realistic imaging condition as used in Table 3, Row 4, and keep it the same for both cases. The validation results on the ARAD1K dataset for existing pre-trained networks are summarized in Table 5. We also visualize the reconstructed spectral images in five arbitrary bands (420 nm, 500 nm, 550 nm, 580 nm, and 660 nm) and spectra of two points in Fig. 4 for Scene ARAD\_1K\_0944 from the validation set.

From the numerical results in Table 5, it is apparent that all the existing methods experience catastrophic performance drop in terms of MRAE and SAM in the presence of metamers, which we call metameric failure. The MRAE (cf. Eq. (4)) may yield large values when big errors occur for dark ground-truth pixels (see the exemplary spectra in Fig. 4). The SAM values become large when the spectra are essentially dissimilar with each other. RMSE and PSNR do not capture the spectral differences as well, since they average out differences in the spatial and spectral dimensions.

The visual results in Fig. 4 show that the reconstruction results are very close to each other for both standard and metamer data, because the input RGB images are quite similar. However, distinct differences exist in the scene for certain spectral bands, e.g., the intensities of the yellow and green parts of the slide (blue box) in 500 nm band

Table 5. Validation performance for different pre-trained models on standard (std) data and metamer (met) adversary synthesized from the ARAD1K dataset [Arad et al. 2022].

Network	Data	MRAE↓	RMSE↓	PSNR↑	SAM↓
MST++	std	0.312	0.055	33.8	0.084
	met	<b>52.839</b>	0.091	26.0	<b>0.580</b>
MST-L	std	0.327	0.055	28.0	0.118
	met	<b>51.321</b>	0.090	25.9	<b>0.579</b>
MPRNet	std	0.661	0.066	26.1	0.125
	met	<b>145.981</b>	0.122	23.3	<b>0.547</b>
Restormer	std	0.510	0.066	25.5	0.126
	met	<b>79.705</b>	0.116	23.4	<b>0.567</b>
MIRNet	std	0.404	0.077	24.8	0.124
	met	<b>38.252</b>	0.089	24.8	<b>0.570</b>
HINet	std	0.450	0.063	26.5	0.120
	met	<b>67.148</b>	0.096	24.8	<b>0.552</b>
HDNet	std	0.450	0.082	23.9	0.126
	met	<b>34.429</b>	0.095	23.8	<b>0.570</b>
AWAN	std	0.424	0.080	24.6	0.119
	met	<b>39.854</b>	0.095	24.4	<b>0.558</b>
EDSR	std	0.421	0.066	25.5	0.132
	met	<b>49.435</b>	0.100	23.8	<b>0.564</b>
HRNet	std	0.514	0.078	23.9	0.128
	met	<b>43.726</b>	0.112	22.7	<b>0.560</b>
HSCNN+	std	0.508	0.075	24.4	0.148
	met	<b>42.274</b>	0.098	23.1	<b>0.556</b>

vary in the standard data, but remain identical in the metamer data. The reconstructions fail to reflect this important difference. All spectral images are displayed on the same global intensity scale, so the brightness differences (green box) in corresponding images reflect the reconstruction artifacts for the metamer data.

### 5.2 Training with metamers

The pre-trained models were not explicitly trained to cope with metamers. This raises the question whether it is possible to improve the performance by training the networks with metamer data.

As a first step, we use both the standard and metamer data ( $\alpha = 0$ ) generated from the ARAD1K dataset to train various networks. To eliminate the impact of other factors, we simulate the RGB images in a noiseless, aberration-free condition, and without compression.

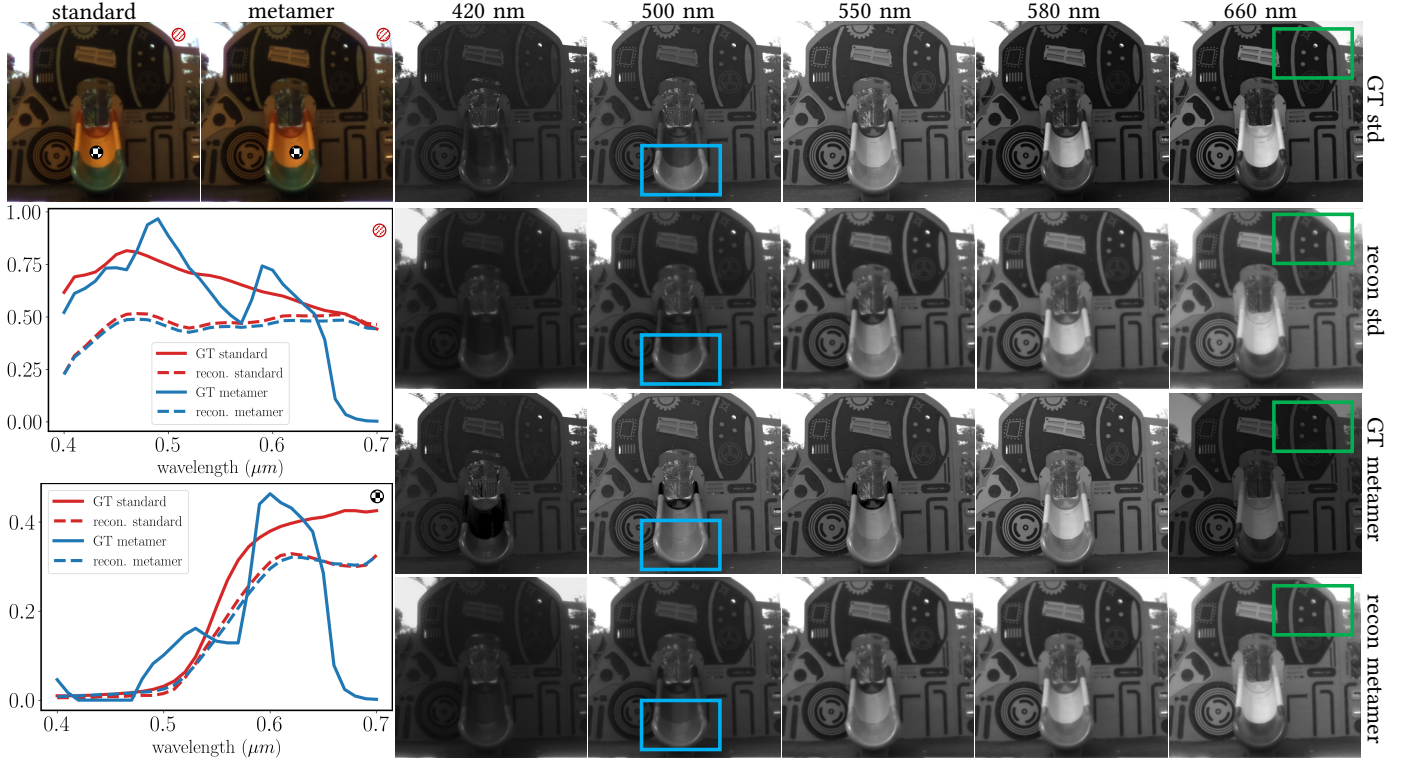


Fig. 4. Validation with metamers for MST++ [Cai et al. 2022b]. An example Scene ARAD\_1K\_0944 is shown to visualize the standard and metamer datacubes. Top left: the standard and metamer data result in similar color images. Bottom left: ground-truth and reconstructed spectra from two labeled points. Right: ground-truth and reconstructed spectral images in 420 nm, 500 nm, 550 nm, 580 nm, and 660 nm.

However, it is not sufficient to consider only a pair of standard and fixed metamer data. In reality, there are infinite metamers that project to the same color. As a second variant, we train the neural networks with random metamers generated on-the-fly as a spectral augmentation to enhance the spectral content of existing datasets. We vary the coefficient for the metameric black by setting  $\alpha$  as a uniformly distributed random number in the range  $[-1, 2]$ . During validation, we use both the standard validation data and their corresponding metamer data with fixed  $\alpha = 0$ , which doubles the amount of the original validation data.

As an example, we train MST++ and evaluate its validation performance over the training process. In Fig. 5, we show that it is no longer a good choice to use MRAE as the loss function [Cai et al. 2022b] and evaluation metric [Arad et al. 2022], because it is completely overwhelmed by metamers. Instead, we find that L1 loss is a more stable loss function, so we train the network with L1 loss for three cases, no metamer (easy), fixed metamer (medium), and on-the-fly metamer (difficult). Nevertheless, we can see in Fig. 5 that the network fails in particular for the spectral accuracy SAM.

We also train all other candidate networks with fixed and on-the-fly metamers. The results are summarized in Table 6. Again, the same performance drop applies to all networks. Finally, we show the results of the top-performing network, MST++ on the CAVE, ICVL, and KAUST datasets in Table 7. (See Supplemental Material

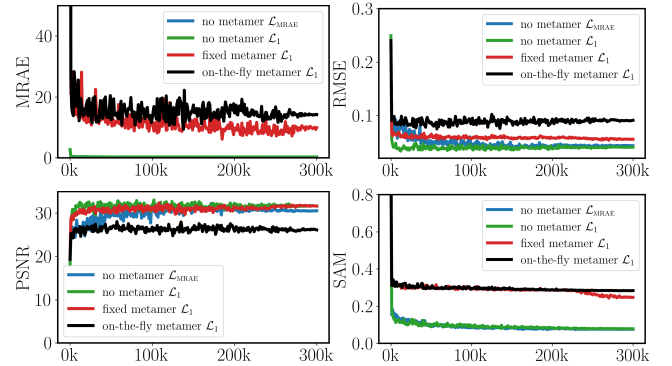


Fig. 5. Training MST++ with metamers. It fails to combat fixed metamers and on-the-fly metamers, in particular on the spectral accuracy SAM.

for more results). As before, the performance drops similarly in the presence of metamers.

### 5.3 Discussion

The experiments conducted in this section clearly highlight the difficulties that the data-driven spectral recovery methods face

Table 6. Performance comparison for training various networks with fixed and on-the-fly metamers.

Network	Metamer	MRAE↓	RMSE↓	PSNR↑	SAM↓
MST++	no	0.270	0.041	31.6	0.079
	fixed	9.912	0.056	31.6	0.247
	on-the-fly	14.224	0.091	26.1	0.284
MST-L	no	0.269	0.040	32.2	0.081
	fixed	11.398	0.061	30.2	0.289
	on-the-fly	12.155	0.061	27.0	0.258
MPRNet	no	0.346	0.051	29.9	0.076
	fixed	7.359	0.059	30.6	0.224
	on-the-fly	13.492	0.087	26.6	0.264
Restormer	no	0.286	0.041	31.5	0.068
	fixed	8.129	0.059	31.0	0.242
	on-the-fly	10.186	0.089	26.7	0.264
MIRNet	no	0.258	0.040	32.2	0.083
	fixed	9.555	0.061	30.5	0.289
	on-the-fly	13.205	0.088	26.4	0.290
HINet	no	0.315	0.056	28.0	0.081
	fixed	8.322	0.068	29.6	0.296
	on-the-fly	14.238	0.090	25.5	0.288
HDNet	no	0.287	0.045	30.2	0.087
	fixed	8.884	0.064	30.2	0.296
	on-the-fly	18.270	0.087	26.4	0.299
AWAN	no	0.240	0.039	32.0	0.073
	fixed	8.789	0.068	29.6	0.294
	on-the-fly	14.406	0.090	26.0	0.264
EDSR	no	0.415	0.061	26.1	0.084
	fixed	9.717	0.073	26.6	0.297
	on-the-fly	11.723	0.101	23.2	0.290
HRNet	no	0.430	0.065	25.6	0.085
	fixed	8.142	0.076	26.0	0.299
	on-the-fly	13.098	0.103	23.0	0.294
HSCNN+	no	0.516	0.077	24.1	0.082
	fixed	9.362	0.085	24.8	0.297
	on-the-fly	13.311	0.102	22.9	0.286

with metamers: (1) **lack of sufficient metameric data** in current datasets, (2) **training with metamers** alone cannot mitigate the issue, and (3) **spectral estimation from RGB data** is indeed limited in the presence of metamers.

The limitations of spectral estimation from RGB data are ultimately not overly surprising – after all the projection from the high dimensional spectral space to RGB invariably destroys scene information that can be difficult to recover. Spatial context from underrepresented data does not contribute to the spectral estimation, because such information remains the same for metamers. However, our experiments show that this is indeed an issue faced by the state-of-the-art methods, which so far went unnoticed due to the under-representation of metamers in the datasets. This shortcoming will also affect other uses of the same datasets, for example in the training of reconstruction methods for spectral computational cameras [Baek et al. 2017; Cao et al. 2011; Jeon et al. 2019]. Metameric adversary helps to identify this overlooked issue, whereas metameric

augmentation has not yet found its way for contribution. We will explore it further in the next section.

Table 7. Training with metamers for MST++ on the CAVE [Yasuma et al. 2010], ICVL [Arad and Ben-Shahar 2016], and KAUST [Li et al. 2021] datasets.

Dataset	Metamer	MRAE↓	RMSE↓	PSNR↑	SAM↓
CAVE	no	1.014	0.038	29.9	0.192
	fixed	38.26	0.053	29.6	0.229
	on-the-fly	226.0	0.078	25.2	0.451
ICVL	no	0.067	0.016	40.1	0.027
	fixed	1.454	0.041	34.8	0.229
	on-the-fly	2.615	0.087	24.3	0.268
KAUST	no	0.082	0.016	43.2	0.076
	fixed	2.033	0.022	39.0	0.217
	on-the-fly	1.874	0.032	33.7	0.245

## 6 FINDING 3: THE ABERRATION ADVANTAGE

As shown so far, the existing methods have difficulties distinguishing metamers in the ideal noiseless and aberration-free condition. In this section, we analyze what effect (if any) optical aberrations have on this situation, *i.e.*, aberration-aware training [Yang et al. 2023]. To this end we train the networks in a realistic imaging condition with moderate noise level ( $npe = 1000$ ), lossless PNG format, and aberrations from the same double Gauss lens as before [Ichimura 2021]. In short, we simulate, through spectral ray tracing, the effect that an imperfect (*i.e.*, aberrated) optical system has on the RGB image measured when observing a specific spectral scene. The details of this simulation can be found in the Supplemental Material.

In Fig. 6, we show an example with MST++ for the validation on SAM in two situations, one with fixed metamers, and the other with on-the-fly metamers. In each experiment, we compare the SAM difference with and without aberrations. As a reference, we also show the standard validation without metamers. As we can see, the realistic optical aberrations of the lens actually *improve* the spectral estimation in the presence of metamers as long as the aberrations are modeled in the training. With chromatic aberrations, the network can already distinguish fixed metamer pairs, achieving similar accuracy as the standard case. In the more aggressive case of on-the-fly metamers, chromatic aberrations also improve the spectral accuracy, compared with its no-aberration counterpart. Again, this aberration advantage holds for all datasets (Table 8). See Supplemental Material for details.

Table 8. SAM metrics for MST++ on CAVE [Yasuma et al. 2010], ICVL [Arad and Ben-Shahar 2016], and KAUST [Li et al. 2021].

Dataset	Fixed metamers		On-the-fly metamers	
	no aberration	aberration	no aberration	aberration
CAVE	0.251	0.135	0.380	0.167
ICVL	0.028	0.077	0.240	0.085
KAUST	0.212	0.113	0.221	0.113

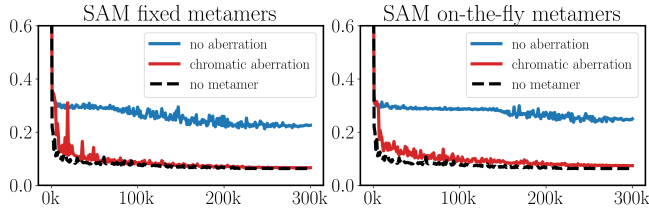


Fig. 6. Chromatic aberrations improve spectral accuracy. Left: fixed metamers. Right: on-the-fly metamers.

## 6.1 Discussion

To understand why optical aberrations help improve the reconstruction, consider the simulated images in Fig. 7. The left and middle images are simulations of RGB images for metameric scene pairs, with the difference image on the right. The different spectra of the two scenes are affected *differently* by the optical aberrations, and therefore, although the *scenes* are metamers of each other, the *RGB images* are in fact different. In effect, the optical aberrations have *encoded* spectral information into the RGB image, which the networks can learn to distinguish, lending credibility to *PSF engineering* methods for hyperspectral encoding [Baek et al. 2017; Cao et al. 2011; Jeon et al. 2019].



Fig. 7. Chromatic aberration induced informative color differences (right) as spectral cues for metamer pairs (left and middle).

There are, however, also detrimental consequences of this effect, namely (1) **“baked-in” aberrations** in spectral datasets and (2) **limited generalization** to arbitrary RGB image sources.

Regarding (1), it is worth noting that even expensive spectral cameras typically do not have diffraction limited optics, *i.e.*, their optical systems are aberrated. In order to avoid overfitting to these aberrations, future datasets should ideally be collected with a large variety of different spectral cameras.

With respect to (2) we note that different RGB cameras produce very different aberrations, and often the aberrations also vary significantly across the image plane. Without further improvements on the reconstruction methods, this will result in a large device dependency and poor generalization of the methods.

## 7 CONCLUSION

In this work, we have comprehensively analyzed a category of data-driven spectral reconstruction methods from RGB images by reviewing the problem fundamentally from dataset bias to physical image formation, and to reconstruction networks. From an optics-aware

perspective, we leverage both metamerism and optical aberrations to reassess existing methodologies.

The major findings of our study are that (1) the limitations of current datasets lead to overfitting to both nuisance parameters (noise, compression), as well as limited scene content. (2) Metamerism in particular presents a challenge both in terms of under-representation in the datasets, and in terms of fundamental limits of spectral reconstruction from RGB input. (3) Metameric augmentation along with the targeted use of optical aberrations enables resolving the metamer issue.

In particular the last point lends additional credibility to computational camera approaches for spectral imaging, including both PSF engineering approaches [Baek et al. 2017; Cao et al. 2011; Jeon et al. 2019] and compressed sensing methods like CASSI [Choi et al. 2017b; Wagadarikar et al. 2008]. However, learned reconstruction methods for these approaches will suffer from the same dataset issues as the methods analyzed in this paper, making the collection of large-scale, diverse spectral image data a matter of urgency.

In order to realize the dream of spectral estimation from arbitrary RGB sources it is necessary to diversify the spectral contents in hyperspectral image datasets and embrace versatile spectral data augmentation methods to fully enable the power of networks in adaptation to whole families of aberrations.

## ACKNOWLEDGMENTS

This work was supported by the King Abdullah University of Science and Technology Individual Baseline Funding. Seung-Hwan Baek was supported by Korea NRF (RS-2023-00211658) and Samsung Electronics.

## REFERENCES

- Eirikur Agustsson and Radu Timofte. 2017. NTIRE 2017 challenge on single image super-resolution: Dataset and study. In *IEEE Conf. Comput. Vis. Pattern Recog. Worksh.* 126–135.
- Arash Akbarinia and Karl R Gegenfurtner. 2018. Color metamerism and the structure of illuminant space. *J. Opt. Soc. Am. A* 35, 4 (2018), B231–B238.
- Ali Alsam and Reiner Lenz. 2007. Calibrating color cameras using metameric blacks. *J. Opt. Soc. Am. A* 24, 1 (2007), 11–17.
- Boaz Arad and Ohad Ben-Shahar. 2016. Sparse recovery of hyperspectral signal from natural RGB images. In *Eur. Conf. Comput. Vis.* Springer, 19–34.
- Boaz Arad, Ohad Ben-Shahar, Radu Timofte, L Van Gool, L Zhang, MH Yang, et al. 2018. NTIRE 2018 challenge on spectral reconstruction from RGB images. In *IEEE Conf. Comput. Vis. Pattern Recog. Worksh.* 1042–1042.
- Boaz Arad, Radu Timofte, Ohad Ben-Shahar, Yi-Tun Lin, and Graham D Finlayson. 2020. NTIRE 2020 challenge on spectral reconstruction from an RGB image. In *IEEE Conf. Comput. Vis. Pattern Recog. Worksh.* 446–447.
- Boaz Arad, Radu Timofte, Rony Yahel, Nimrod Morag, Amir Bernat, Yuanhao Cai, Jing Lin, Zudi Lin, Haoqian Wang, Yulun Zhang, et al. 2022. NTIRE 2022 spectral recovery challenge and data set. In *IEEE Conf. Comput. Vis. Pattern Recog. Worksh.* 863–881.
- Henry Arguello, Samuel Pinilla, Yifan Peng, Hayato Ikoma, Jorge Bacca, and Gordon Wetzstein. 2021. Shift-variant color-coded diffractive spectral imaging system. *Optica* 8, 11 (2021), 1424–1434.
- Seung-Hwan Baek, Incheol Kim, Diego Gutierrez, and Min H Kim. 2017. Compact single-shot hyperspectral imaging using a prism. *ACM Trans. Graph.* 36, 6 (2017), 1–12.
- Bikram Pratap Banerjee, Simit Raval, and PJ Cullen. 2020. UAV-hyperspectral imaging of spectrally complex environments. *Int. J. Remote Sens.* 41, 11 (2020), 4136–4159.
- Mohammad Mahdi Bejani and Mehdi Ghatee. 2021. A systematic review on overfitting control in shallow and deep neural networks. *Artif. Intell. Rev.* (2021), 1–48.
- L. Belcour, P. Barla, and G. Guennebaud. 2023. One-to-Many Spectral Upsampling of Reflectances and Transmittances. *Comput. Graph. Forum* 42, 4 (2023), e14886.
- Yuanhao Cai, Jing Lin, Xiaowan Hu, Haoqian Wang, Xin Yuan, Yulun Zhang, Radu Timofte, and Luc Van Gool. 2022a. Mask-guided spectral-wise transformer for

- efficient hyperspectral image reconstruction. In *IEEE Conf. Comput. Vis. Pattern Recog.* 17502–17511.
- Yuanhao Cai, Jing Lin, Zudi Lin, Haoqian Wang, Yulun Zhang, Hanspeter Pfister, Radu Timofte, and Luc Van Gool. 2022b. MST++: Multi-stage spectral-wise transformer for efficient spectral reconstruction. In *IEEE Conf. Comput. Vis. Pattern Recog. Worksh.* 745–755.
- Xun Cao, Hao Du, Xin Tong, Qionghai Dai, and Stephen Lin. 2011. A prism-mask system for multispectral video acquisition. *IEEE Trans. Pattern Anal. Mach. Intell.* 33, 12 (2011), 2423–2435.
- Ayan Chakrabarti and Todd Zickler. 2011. Statistics of real-world hyperspectral images. In *IEEE Conf. Comput. Vis. Pattern Recog.* IEEE, 193–200.
- Liangyu Chen, Xin Lu, Jie Zhang, Xiaojie Chu, and Chengpeng Chen. 2021. HINet: Half instance normalization network for image restoration. In *IEEE Conf. Comput. Vis. Pattern Recog.* 182–192.
- Inchang Choi, Daniel S. Jeon, Giljoo Nam, Diego Gutierrez, and Min H. Kim. 2017a. High-Quality Hyperspectral Reconstruction Using a Spectral Prior. *ACM Trans. Graph.* 36, 6 (2017), 218:1–13.
- Inchang Choi, MH Kim, D Gutierrez, DS Jeon, and G Nam. 2017b. High-quality hyperspectral reconstruction using a spectral prior. *ACM Trans. Graph.* 36, 6 (2017), 1–13.
- Jozef B Cohen and William E Kappauf. 1982. Metameric color stimuli, fundamental metamers, and Wyszecki’s metameric blacks. *Am. J. Psychol.* (1982), 537–564.
- William J Cukierski and David J Foran. 2010. Metamerism in multispectral imaging of histopathology specimens. In *2010 IEEE International Symposium on Biomedical Imaging: From Nano to Macro.* IEEE, 145–148.
- Laura M Dale, André Thewis, Christelle Boudry, Ioan Rotar, Pierre Dardenne, Vincent Baeten, and Juan A Fernández Pierna. 2013. Hyperspectral imaging applications in agriculture and agro-food product quality and safety control: A review. *Appl. Spectrosc. Rev.* 48, 2 (2013), 142–159.
- Jia Deng, Wei Dong, Richard Socher, Li-Jia Li, Kai Li, and Li Fei-Fei. 2009. ImageNet: A large-scale hierarchical image database. In *IEEE Conf. Comput. Vis. Pattern Recog.* Ieee, 248–255.
- Simone Fabbrizzi, Symeon Papadopoulos, Eirini Ntoutsis, and Ioannis Kompatsiaris. 2022. A survey on bias in visual datasets. *Comput. Vis. Image Underst.* 223 (2022), 103552.
- Mathieu Fauvel, Yuliya Tarabalka, Jon Atli Benediktsson, Jocelyn Chanussot, and James C Tilton. 2012. Advances in spectral-spatial classification of hyperspectral images. *Proc. IEEE* 101, 3 (2012), 652–675.
- Graham D Finlayson and Peter Morovic. 2005. Metamer sets. *J. Opt. Soc. Am. A* 22, 5 (2005), 810–819.
- David H Foster and Kinjiro Amano. 2019. Hyperspectral imaging in color vision research: tutorial. *J. Opt. Soc. Am. A* 36, 4 (2019), 606–627.
- David H Foster, Kinjiro Amano, Sérgio MC Nascimento, and Michael J Foster. 2006. Frequency of metamerism in natural scenes. *J. Opt. Soc. Am. A* 23, 10 (2006), 2359–2372.
- Bernhard Hill. 1999. Color capture, color management, and the problem of metamerism: does multispectral imaging offer the solution?. In *Proc. SPIE*, Vol. 3963. SPIE, 2–14.
- Bernhard Hill. 2002. Optimization of total multispectral imaging systems: best spectral match versus least observer metamerism. In *Proc. SPIE*, Vol. 4421. SPIE, 481–486.
- Xiaowan Hu, Yuanhao Cai, Jing Lin, Haoqian Wang, Xin Yuan, Yulun Zhang, Radu Timofte, and Luc Van Gool. 2022. HDNet: High-resolution dual-domain learning for spectral compressive imaging. In *IEEE Conf. Comput. Vis. Pattern Recog.* 17542–17551.
- Longqian Huang, Ruichen Luo, Xu Liu, and Xiang Hao. 2022. Spectral imaging with deep learning. *Light Sci. Appl.* 11, 1 (2022), 61.
- Junya Ichimura. 2021. Optical system and image pickup apparatus having the same. US Patent App. 17/174,832.
- Roman Jacome, Pablo Gomez, and Henry Arguello. 2023. Middle output regularized end-to-end optimization for computational imaging. *Optica* 10, 11 (2023), 1421–1431.
- Wenzel Jakob and Johannes Hanika. 2019. A low-dimensional function space for efficient spectral upsampling. In *Comput. Graph. Forum*, Vol. 38. Wiley Online Library, 147–155.
- Daniel S Jeon, Seung-Hwan Baek, Shinyoung Yi, Qiang Fu, Xiong Dun, Wolfgang Heidrich, and Min H Kim. 2019. Compact snapshot hyperspectral imaging with diffracted rotation. *ACM Trans. Graph.* 38, 4 (2019), 1–13.
- Yuhyun Ji, Sang Mok Park, Semin Kwon, Jung Woo Leem, Vidhya Vijayakrishnan Nair, Yunjie Tong, and Young L Kim. 2023. mHealth hyperspectral learning for instantaneous spatiotemporal imaging of hemodynamics. *Proc. Natl. Acad. Sci.* 2, 4 (2023), pggad111.
- Min H Kim. 2013. 3D graphics techniques for capturing and inspecting hyperspectral appearance. In *2013 International Symposium on Ubiquitous Virtual Reality.* IEEE, 15–18.
- Simon Kornblith, Jonathon Shlens, and Quoc V Le. 2019. Do better ImageNet models transfer better?. In *IEEE Conf. Comput. Vis. Pattern Recog.* 2661–2671.
- Sarawak Kuching. 2007. The performance of maximum likelihood, spectral angle mapper, neural network and decision tree classifiers in hyperspectral image analysis. *J. Comput. Sci.* 3, 6 (2007), 419–423.
- Jiaojiao Li, Chaoyong Wu, Rui Song, Yunsong Li, and Fei Liu. 2020. Adaptive weighted attention network with camera spectral sensitivity prior for spectral reconstruction from RGB images. In *IEEE Conf. Comput. Vis. Pattern Recog. Worksh.* 462–463.
- Yuqi Li, Qiang Fu, and Wolfgang Heidrich. 2021. Multispectral illumination estimation using deep unrolling network. In *Int. Conf. Comput. Vis.* 2672–2681.
- Bee Lim, Sanghyun Son, Heewon Kim, Seungjun Nah, and Kyoung Mu Lee. 2017. Enhanced deep residual networks for single image super-resolution. In *IEEE Conf. Comput. Vis. Pattern Recog. Worksh.* 136–144.
- Vaibhav Lodhi, Debashish Chakravarty, and Pabitra Mitra. 2019. Hyperspectral imaging system: Development aspects and recent trends. *Sens. Imaging* 20 (2019), 1–24.
- Guolan Lu and Baowei Fei. 2014. Medical hyperspectral imaging: a review. *J. Biomed. Opt.* 19, 1 (2014), 010901–010901.
- Yusuke Monno, Sunao Kikuchi, Masayuki Tanaka, and Masatoshi Okutomi. 2015. A practical one-shot multispectral imaging system using a single image sensor. *IEEE Trans. Image Process.* 24, 10 (2015), 3048–3059.
- Samuel Ortega, Martin Halicek, Himar Fabelo, Gustavo M Callico, and Baowei Fei. 2020. Hyperspectral and multispectral imaging in digital and computational pathology: a systematic review. *Biomed. Opt. Express* 11, 6 (2020), 3195–3233.
- Bosoon Park, WR Windham, KC Lawrence, and DP Smith. 2007. Contaminant classification of poultry hyperspectral imagery using a spectral angle mapper algorithm. *Biosyst. Eng.* 96, 3 (2007), 323–333.
- Matt Pharr, Wenzel Jakob, and Greg Humphreys. 2023. *Physically based rendering: From theory to implementation.* MIT Press.
- Dilip K Prasad and Looi Wenhe. 2015. Metrics and statistics of frequency of occurrence of metamerism in consumer cameras for natural scenes. *J. Opt. Soc. Am. A* 32, 7 (2015), 1390–1402.
- Aneesh Rangnekar, Zachary Mulhollan, Anthony Vodacek, Matthew Hoffman, Angel D Sappa, Erik Blasch, Jun Yu, Liwen Zhang, Shenshen Du, Hao Chang, et al. 2022. Semi-Supervised Hyperspectral Object Detection Challenge Results-PBVS 2022. In *IEEE Conf. Comput. Vis. Pattern Recog.* 390–398.
- Sylvestre-Alvise Rebuffi, Sven Gowal, Dan Andrei Calian, Florian Stimberg, Olivia Wiles, and Timothy A Mann. 2021. Data augmentation can improve robustness. *Adv. Neural Inf. Process.* 34 (2021), 29935–29948.
- Vishwanath Saragadam and Aswin C Sankaranarayanan. 2019. KRISM—Krylov subspace-based optical computing of hyperspectral images. *ACM Trans. Graph.* 38, 5 (2019), 1–14.
- Zhan Shi, Chang Chen, Zhiwei Xiong, Dong Liu, and Feng Wu. 2018. HSCNN+: Advanced CNN-based hyperspectral recovery from RGB images. In *IEEE Conf. Comput. Vis. Pattern Recog. Worksh.* 939–947.
- Connor Shorten and Taghi M Khoshgoftaar. 2019. A survey on image data augmentation for deep learning. *J. Big Data* 6, 1 (2019), 1–48.
- William A Thornton. 1998. How strong metamerism disturbs color spaces. *Color Res. Appl.* 23, 6 (1998), 402–407.
- Antonio Torralba and Alexei A Efros. 2011. Unbiased look at dataset bias. In *IEEE Conf. Comput. Vis. Pattern Recog.* IEEE, 1521–1528.
- Mark Van De Ruit and Elmar Eisemann. 2023. Metameric: Spectral Uplifting via Controllable Color Constraints. In *ACM SIGGRAPH 2023 Conference Proceedings.* Article 42, 10 pages.
- Freek Van der Meer. 2006. The effectiveness of spectral similarity measures for the analysis of hyperspectral imagery. *Int. J. Appl. Earth Obs. Geoinf.* 8, 1 (2006), 3–17.
- Cornelius van Trigt. 1994. Metameric blacks and estimating reflectance. *J. Opt. Soc. Am. A* 11, 3 (1994), 1003–1024.
- Françoise Viénot and Hans Brettel. 2014. The Verriest Lecture: Visual properties of metameric blacks beyond cone vision. *J. Opt. Soc. Am. A* 31, 4 (2014), A38–A46.
- Ashwin Wagadarikar, Renu John, Rebecca Willett, and David Brady. 2008. Single disperser design for coded aperture snapshot spectral imaging. *Appl. Opt.* 47, 10 (2008), B44–B51.
- Andrea Weidlich, Alex Forsythe, Scott Dyer, Thomas Mansencal, Johannes Hanika, Alexander Wilkie, Luke Emrose, and Anders Langlands. 2021. Spectral imaging in production: course notes SIGGRAPH 2021. In *ACM SIGGRAPH 2021 Courses.* Association for Computing Machinery (ACM), 1–90.
- Roman Werpachowski, András György, and Csaba Szepesvári. 2019. Detecting overfitting via adversarial examples. *Adv. Neural Inf. Process.* 32 (2019).
- Hao Xu, Shiqi Chen, Haiquan Hu, Peng Luo, Zheyang Jin, Qi Li, Zhihai Xu, Huajun Feng, Yueting Chen, and Tingting Jiang. 2024. Wavelength encoding spectral imaging based on the combination of deeply learned filters and an RGB camera. *Opt. Express* 32, 7 (2024), 10741–10760.
- Xinge Yang, Qiang Fu, Mohamed Elhoseiny, and Wolfgang Heidrich. 2023. Aberration-aware depth-from-focus. *IEEE Trans. Pattern Anal. Mach. Intell.* (2023).
- Fumihito Yasuma, Tomoo Mitsunaga, Daisuke Iso, and Shree K Nayar. 2010. Generalized assorted pixel camera: postcapture control of resolution, dynamic range, and spectrum. *IEEE Trans. Image Process.* 19, 9 (2010), 2241–2253.
- Syed Waqas Zamir, Aditya Arora, Salman Khan, Munawar Hayat, Fahad Shahbaz Khan, and Ming-Hsuan Yang. 2022. Restormer: Efficient transformer for high-resolution image restoration. In *IEEE Conf. Comput. Vis. Pattern Recog.* 5728–5739.

- Syed Waqas Zamir, Aditya Arora, Salman Khan, Munawar Hayat, Fahad Shahbaz Khan, Ming-Hsuan Yang, and Ling Shao. 2020. Learning enriched features for real image restoration and enhancement. In *Eur. Conf. Comput. Vis.* Springer, 492–511.
- Syed Waqas Zamir, Aditya Arora, Salman Khan, Munawar Hayat, Fahad Shahbaz Khan, Ming-Hsuan Yang, and Ling Shao. 2021. Multi-stage progressive image restoration. In *IEEE Conf. Comput. Vis. Pattern Recog.* 14821–14831.
- Jingang Zhang, Runmu Su, Qiang Fu, Wenqi Ren, Felix Heide, and Yunfeng Nie. 2022. A survey on computational spectral reconstruction methods from RGB to hyperspectral imaging. *Sci. Rep.* 12, 1 (2022), 11905.
- Yuzhi Zhao, Lai-Man Po, Qiong Yan, Wei Liu, and Tingyu Lin. 2020. Hierarchical regression network for spectral reconstruction from RGB images. In *IEEE Conf. Comput. Vis. Pattern Recog. Worksh.* 422–423.

## APPENDIX

### A IMAGE FORMATION MODEL

Mathematically, the physical image formation of a color image from the spectral radiance can be expressed by

$$g_c(x, y) = \int_{\lambda_1}^{\lambda_2} (f(x, y, \lambda) * h(x, y, \lambda)) q_c(\lambda) d\lambda, \quad (9)$$

where  $f(x, y, \lambda)$  is the spectral image,  $h(x, y, \lambda)$  is the spectral point spread function (PSF) of the optical system,  $q_c(\lambda)$  is the spectral response function (SRF) of the sensor, and  $g_c(x, y)$  is the color image in color channel  $c \in [R, G, B]$ .

Let us denote the hyperspectral image as a matrix  $\mathbf{X} \in \mathbb{R}^{MN \times K}$ , where  $M, N$  are the number of pixels in spatial dimensions, and  $K$  is the number of spectral bands in spectral dimension. Note that we have stacked the 2D spectral images in rows of  $\mathbf{X}$ . Explicitly, we have

$$\mathbf{X} = [\mathbf{x}_1, \mathbf{x}_2, \dots, \mathbf{x}_K], \quad (10)$$

where each column  $\mathbf{x}_k \in \mathbb{R}^{MN \times 1}$  is a vector for the spectral image in spectral channel  $k$ . The SRF of the sensor is a matrix  $\mathbf{Q} \in \mathbb{R}^{K \times 3}$ , *i.e.*,

$$\mathbf{Q} = [\mathbf{q}_1, \mathbf{q}_2, \mathbf{q}_3] = \begin{bmatrix} q_{11} & q_{21} & q_{31} \\ q_{21} & q_{22} & q_{32} \\ \vdots & \ddots & \vdots \\ q_{K1} & q_{K2} & q_{K3} \end{bmatrix}, \quad (11)$$

where each column  $\mathbf{q}_c \in \mathbb{R}^{K \times 1}$ . Therefore, the spectrum-to-color projection results in a color image

$$\mathbf{Y} = \mathbf{X}\mathbf{Q}, \quad (12)$$

where  $\mathbf{Y} \in \mathbb{R}^{MN \times 3}$  with three columns

$$\mathbf{Y} = [\mathbf{y}_1, \mathbf{y}_2, \mathbf{y}_3], \quad (13)$$

and each column  $\mathbf{y}_c \in \mathbb{R}^{MN \times 1}$  is a vector for the image in color channel  $c \in [R, G, B]$ .

When considering the spectral PSFs in each spectral channel, the optically blurred image can be expressed by

$$\mathbf{w}_k = \mathbf{A}_k \mathbf{x}_k, \quad k \in [1, 2, \dots, K], \quad (14)$$

where  $\mathbf{A}_k \in \mathbb{R}^{MN \times MN}$  is a matrix that represents the spectral PSF in channel  $k$ . Similar as  $\mathbf{X}$ , we concatenate  $\mathbf{w}_k$  horizontally to obtain the spectral images through the optical system as

$$\begin{aligned} \mathbf{W} &= [\mathbf{w}_1, \mathbf{w}_2, \dots, \mathbf{w}_K] \\ &= [\mathbf{A}_1 \mathbf{x}_1, \mathbf{A}_2 \mathbf{x}_2, \dots, \mathbf{A}_K \mathbf{x}_K]. \end{aligned} \quad (15)$$

We define a block matrix

$$\mathbf{A} = \begin{bmatrix} \mathbf{A}_1 \\ \mathbf{A}_2 \\ \vdots \\ \mathbf{A}_K \end{bmatrix}, \quad (16)$$

which stacks the matrices  $\mathbf{A}_k$  vertically, and  $\mathbf{A} \in \mathbb{R}^{KMN \times MN}$ . Therefore, we have

$$\mathbf{W} = \text{diag}(\mathbf{A}\mathbf{X}), \quad (17)$$

where  $\text{diag}(\cdot)$  extracts the  $K$  diagonal blocks and concatenate them horizontally,

$$\begin{aligned} \mathbf{A}\mathbf{X} &= \begin{bmatrix} \mathbf{A}_1 \\ \mathbf{A}_2 \\ \vdots \\ \mathbf{A}_K \end{bmatrix} [\mathbf{x}_1, \mathbf{x}_2, \dots, \mathbf{x}_K] \\ &= \begin{bmatrix} \mathbf{A}_1 \mathbf{x}_1 & \mathbf{A}_1 \mathbf{x}_2 & \cdots & \mathbf{A}_1 \mathbf{x}_K \\ \mathbf{A}_2 \mathbf{x}_1 & \mathbf{A}_2 \mathbf{x}_2 & \cdots & \mathbf{A}_2 \mathbf{x}_K \\ \vdots & \vdots & \ddots & \vdots \\ \mathbf{A}_K \mathbf{x}_1 & \mathbf{A}_K \mathbf{x}_2 & \cdots & \mathbf{A}_K \mathbf{x}_K \end{bmatrix}. \end{aligned} \quad (18)$$

Finally, the color image is

$$\mathbf{Z} = \mathbf{W}\mathbf{Q} = \text{diag}(\mathbf{A}\mathbf{X})\mathbf{Q}. \quad (19)$$

where  $\mathbf{Z} = [\mathbf{z}_1, \mathbf{z}_2, \mathbf{z}_3] \in \mathbb{R}^{MN \times 3}$ .

### B EFFECT OF CLIPPING TO NON-NEGATIVE VALUES.

It is necessary to clip negative values in the generated metamer data to ensure the resulting spectra are physically plausible (*i.e.*, no negative spectral radiance). This may lead to slight deviations in the RGB values, and therefore images that are not *exact* metamers. However, we verify that the resulting difference is actually negligible by comparing the projected RGB images from the metamer pairs. For example, in the experiments of Table 5 in the main paper, 32.9% of the generated metamers produce exactly the same RGB images (exact-metamers). Among the remaining 67.1% that are affected by clipping (*i.e.*, near-metamers), the average PSNR between the RGB pairs is 75.8 dB, with a standard deviation of  $\pm 17.7$  dB. This indicates that the effect of clipping the negative values in the metamer spectra is negligible.

# Limitations of Data-Driven Spectral Reconstruction – Optics-Aware Analysis and Mitigation Supplemental Material

QIANG FU\* and MATHEUS SOUZA\*, KAUST, Saudi Arabia

EUNSUE CHOI, SUHYUN SHIN, and SEUNG-HWAN BAEK, POSTECH, Korea

WOLFGANG HEIDRICH, KAUST, Saudi Arabia

CCS Concepts: • **Computing methodologies** → **Hyperspectral imaging**; **Computational photography**.

## ACM Reference Format:

Qiang Fu, Matheus Souza, Eunsue Choi, Suhyun Shin, Seung-Hwan Baek, and Wolfgang Heidrich. 2024. Limitations of Data-Driven Spectral Reconstruction – Optics-Aware Analysis and Mitigation Supplemental Material. 1, 1 (April 2024), 10 pages. <https://doi.org/10.1145/nnnnnnn.nnnnnnn>

## 1 ABERRATED SPECTRAL PSFS

In Supplemental Fig. S1, we show the schematic optical layout of the double Gauss lens [Ichimura 2021] we use throughout the experiments. It consists of 6 lens elements with an aperture stop in the middle. The effective focal length is 50 mm, and the F-number is F/1.8. We model the spectral PSFs at each wavelength in the spectral range [400 nm, 700 nm] with a step size of 10 nm in the optical design software ZEMAX (v14.2) by spectral ray tracing. The sensor parameters are set according to the specifications of Basler ace 2 camera (model A2a5320-23ucBAS), as used in the NTIRE 2022 spectral recovery challenge [Arad et al. 2022]. In Supplemental Fig. S1, we render the corresponding spectral PSFs in color with the SRF of that sensor. Although the lens is well designed to minimize all kinds of aberrations, clear chromatic aberrations can still be observed, in particular in the short (blue) and long (red) ends of the spectral bands. It is impossible to completely *eliminate* aberrations in photographic lenses [Fischer et al. 2000; Smith 2008]. Note that all the spectral PSFs are normalized by their own maximum values for visualization purpose only.

\*Both authors contributed equally to this research.

Authors' addresses: Qiang Fu, [qiang.fu@kaust.edu.sa](mailto:qiang.fu@kaust.edu.sa); Matheus Souza, [matheus.medeirosdesouza@kaust.edu.sa](mailto:matheus.medeirosdesouza@kaust.edu.sa), KAUST, Thuwal, Saudi Arabia, 23955-6900; Eunsue Choi, [ches7283@postech.ac.kr](mailto:ches7283@postech.ac.kr); Suhyun Shin, [shshin9812@postech.ac.kr](mailto:shshin9812@postech.ac.kr); Seung-Hwan Baek, [shwbaek@postech.ac.kr](mailto:shwbaek@postech.ac.kr), POSTECH, Pohang, Korea, 37673; Wolfgang Heidrich, KAUST, Thuwal, Saudi Arabia, [wolfgang.heidrich@kaust.edu.sa](mailto:wolfgang.heidrich@kaust.edu.sa).

Permission to make digital or hard copies of all or part of this work for personal or classroom use is granted without fee provided that copies are not made or distributed for profit or commercial advantage and that copies bear this notice and the full citation on the first page. Copyrights for components of this work owned by others than the author(s) must be honored. Abstracting with credit is permitted. To copy otherwise, or republish, to post on servers or to redistribute to lists, requires prior specific permission and/or a fee. Request permissions from [permissions@acm.org](mailto:permissions@acm.org).

© 2024 Copyright held by the owner/author(s). Publication rights licensed to ACM.

ACM XXXX-XXXX/2024/4-ART

<https://doi.org/10.1145/nnnnnnn.nnnnnnn>

## 2 RESULTS OF TRAINING WITH LESS DATA FOR OTHER NETWORKS

In Table 2 of the main paper, we summarize that the performance of all the candidate networks on the ARAD1K dataset is mildly affected by using only half of the training data. The detailed validation results over the course of training are shown in Supplemental Fig. S2 and Fig. S3. Here we show extended experimental results for the effects of training with 100%, 50%, and 20% of the full training data. All the results consistently support our indication of lack of diversity in the dataset.

## 3 RESULTS OF VALIDATION WITH UNSEEN DATA FOR OTHER NETWORKS

In Table 3 of the main paper, we demonstrate the performance drop behaviour of the MST++ network on the ARAD1K dataset. To prove that this is true to other networks as well, we carry out the same experiments for all the other candidate networks. The results are summarized in Supplemental Table S.I. As the noise levels, RGB formats, and aberration conditions asymptotically approach realistic imaging scenarios in the real world, the pre-trained models [Cai et al. 2022b] for other networks gradually degrade, similar as the MST++. All the results consistently support our conclusion about the generalization difficulties of these methods in realistic imaging conditions.

## 4 RESULTS OF CROSS-DATASET VALIDATION FOR OTHER NETWORKS

As shown in Tabel 4 in the main paper, we demonstrate that the MST++ network has difficulties in keeping high performance when it is trained on one dataset and validated on another dataset. In Supplemental Table S.II, we show with extended experimental results that the effects of cross-dataset validation are true for all other networks as well. Similar cross-dataset failure can be observed for all the candaidate networks. These results consistently support our conclusion about the the important roles of scene content and acquisition devices in different datasets.

## 5 RESULTS OF METAMER FAILURE FOR OTHER DATASETS

In Table 6 of the main paper, we compare the performance of the candidate networks for the standard data (no metamers), fixed metamers ( $\alpha = 0$ ), and on-the-fly metamers ( $\alpha$  varies in the range of [-1, 2] during training) synthesized from the ARAD1K dataset. All the metrics degrade significantly in the presence of metamers. In Supplemental Table S.III and Table S.IV, we further show that this is also true for

Table S.I. Evaluation of pre-trained models on synthesized validation data generated from the ARAD1K dataset.

Network	Data property				MRAE ↓	RMSE ↓	PSNR ↑	SAM ↓
	Data source	Noise (npe)	RGB format	Aberration				
MST++	NTIRE 2022	unknown	jpg (Q unknown)	None	0.170	0.029	33.8	0.084
	Synthesized	0	jpg (Q = 65)	None	0.460	0.049	29.2	0.094
		0	png (lossless)	None	0.362	0.057	28.7	0.087
		1000	png (lossless)	CA*	0.312	0.055	28.4	0.118
MST-L	NTIRE 2022	unknown	jpg (Q unknown)	None	0.181	0.031	33.0	0.091
	Synthesize	0	jpg (Q = 65)	None	0.417	0.047	29.7	0.099
		0	png (lossless)	None	0.384	0.058	28.4	0.096
		1000	png (lossless)	CA*	0.327	0.055	28.0	0.118
MPRNet	NTIRE 2022	unknown	jpg (Q unknown)	None	0.182	0.032	32.9	0.088
	Synthesize	0	jpg (Q = 65)	None	0.453	0.048	29.1	0.092
		0	png (lossless)	None	0.359	0.051	29.5	0.086
		1000	png (lossless)	CA*	0.661	0.066	26.1	0.125
Restormer	NTIRE 2022	unknown	jpg (Q unknown)	None	0.190	0.032	33.0	0.097
	Synthesize	0	jpg (Q = 65)	None	0.454	0.051	28.6	0.100
		0	png (lossless)	None	0.363	0.053	28.6	0.098
		1000	png (lossless)	CA*	0.510	0.066	25.5	0.126
MIRNet	NTIRE 2022	unknown	jpg (Q unknown)	None	0.189	0.032	33.3	0.091
	Synthesize	0	jpg (Q = 65)	None	0.467	0.051	28.7	0.096
		0	png (lossless)	None	0.366	0.055	28.8	0.091
		1000	png (lossless)	CA*	0.404	0.077	24.8	0.124
HINet	NTIRE 2022	unknown	jpg (Q unknown)	None	0.212	0.037	31.4	0.091
	Synthesize	0	jpg (Q = 65)	None	0.460	0.051	28.3	0.094
		0	png (lossless)	None	0.384	0.055	28.2	0.094
		1000	png (lossless)	CA*	0.450	0.063	26.5	0.120
HDNet	NTIRE 2022	unknown	jpg (Q unknown)	None	0.214	0.037	31.5	0.098
	Synthesize	0	jpg (Q = 65)	None	0.404	0.050	28.8	0.102
		0	png (lossless)	None	0.395	0.057	28.0	0.096
		1000	png (lossless)	CA*	0.450	0.082	23.9	0.126
AWAN	NTIRE 2022	unknown	jpg (Q unknown)	None	0.222	0.041	31.0	0.098
	Synthesize	0	jpg (Q = 65)	None	0.299	0.044	29.7	0.105
		0	png (lossless)	None	0.338	0.060	28.3	0.090
		1000	png (lossless)	CA*	0.424	0.080	24.6	0.119
EDSR	NTIRE 2022	unknown	jpg (Q unknown)	None	0.340	0.051	27.5	0.095
	Synthesize	0	jpg (Q = 65)	None	0.473	0.064	25.8	0.104
		0	png (lossless)	None	0.474	0.074	24.5	0.096
		1000	png (lossless)	CA*	0.421	0.066	25.5	0.132
HRNet	NTIRE 2022	unknown	jpg (Q unknown)	None	0.376	0.065	25.4	0.102
	Synthesize	0	jpg (Q = 65)	None	0.397	0.066	25.3	0.108
		0	png (lossless)	None	0.411	0.070	25.0	0.101
		1000	png (lossless)	CA*	0.514	0.078	23.9	0.128
HSCNN+	NTIRE 2022	unknown	jpg (Q unknown)	None	0.391	0.067	25.5	0.105
	Synthesize	0	jpg (Q = 65)	None	0.490	0.073	24.5	0.113
		0	png (lossless)	None	0.485	0.080	23.9	0.101
		1000	png (lossless)	CA*	0.508	0.075	24.4	0.148

\*CA: chromatic aberration, from a patent double Gauss lens (US20210263286A1).

Table S.II. Cross-dataset validation for all networks.

		MST++[Cai et al. 2022b]				MST-L[Cai et al. 2022a]			
Trained on	Validated on	MRAE↓	RMSE↓	PSNR↑	SAM↓	MRAE↓	RMSE↓	PSNR↑	SAM↓
CAVE	CAVE	0.237	0.034	31.9	0.194	0.234	0.031	32.0	0.187
ARAD1K	CAVE	1.626	0.074	24.4	0.376	2.055	0.070	25.3	0.367
ICVL	ICVL	0.079	0.019	38.3	0.024	0.063	0.015	41.1	0.023
ARAD1K	ICVL	1.032	0.188	19.3	0.924	0.349	0.052	27.8	0.100
KAUST	KAUST	0.069	0.013	44.4	0.061	0.082	0.016	43.8	0.070
ARAD1K	KAUST	1.042	0.100	22.0	0.370	1.114	0.115	21.8	0.370
		MPRNet[Zamir et al. 2021]				Restormer[Zamir et al. 2022]			
Trained on	Validated on	MRAE↓	RMSE↓	PSNR↑	SAM↓	MRAE↓	RMSE↓	PSNR↑	SAM↓
CAVE	CAVE	0.295	0.045	29.4	0.173	0.246	0.036	30.0	0.177
ARAD1K	CAVE	2.063	0.060	26.4	0.378	1.689	0.060	26.5	0.375
ICVL	ICVL	0.077	0.018	39.9	0.024	0.084	0.020	37.4	0.026
ARAD1K	ICVL	0.349	0.050	27.5	0.100	0.347	0.052	27.4	0.097
KAUST	KAUST	0.170	0.022	35.8	0.071	0.067	0.014	44.9	0.066
ARAD1K	KAUST	0.885	0.101	23.1	0.350	1.496	0.144	20.0	0.363
		MIRNet[Zamir et al. 2020]				HINet[Chen et al. 2021]			
Trained on	Validated on	MRAE↓	RMSE↓	PSNR↑	SAM↓	MRAE↓	RMSE↓	PSNR↑	SAM↓
CAVE	CAVE	0.214	0.027	33.6	0.177	0.283	0.041	29.4	0.191
ARAD1K	CAVE	2.039	0.075	24.9	0.406	1.512	0.084	23.3	0.393
ICVL	ICVL	0.060	0.013	40.8	0.023	0.087	0.021	36.2	0.028
ARAD1K	ICVL	0.365	0.052	27.5	0.114	0.387	0.058	26.2	0.127
KAUST	KAUST	0.079	0.015	42.9	0.070	0.089	0.017	42.2	0.074
ARAD1K	KAUST	1.642	0.154	19.4	0.357	1.393	0.140	19.8	0.362
		HDNet[Hu et al. 2022]				AWAN[Li et al. 2020]			
Trained on	Validated on	MRAE↓	RMSE↓	PSNR↑	SAM↓	MRAE↓	RMSE↓	PSNR↑	SAM↓
CAVE	CAVE	0.266	0.041	29.1	0.199	0.305	0.057	28.0	0.237
ARAD1K	CAVE	1.564	0.078	23.9	0.406	1.743	0.077	24.7	0.397
ICVL	ICVL	0.076	0.018	37.4	0.028	0.083	0.018	38.6	0.026
ARAD1K	ICVL	0.598	0.085	22.3	0.129	0.408	0.060	26.5	0.108
KAUST	KAUST	0.076	0.015	42.0	0.070	0.083	0.015	41.0	0.063
ARAD1K	KAUST	1.389	0.142	19.6	0.394	1.844	0.174	18.7	0.370
		EDSR[Lim et al. 2017]				HRNet[Zhao et al. 2020]			
Trained on	Validated on	MRAE↓	RMSE↓	PSNR↑	SAM↓	MRAE↓	RMSE↓	PSNR↑	SAM↓
CAVE	CAVE	0.308	0.058	26.1	0.194	0.317	0.058	26.7	0.196
ARAD1K	CAVE	1.757	0.078	23.4	0.416	1.170	0.076	23.8	0.389
ICVL	ICVL	0.111	0.030	33.0	0.027	0.103	0.026	33.8	0.028
ARAD1K	ICVL	0.474	0.067	24.2	0.119	0.531	0.075	23.3	0.115
KAUST	KAUST	0.215	0.037	31.6	0.081	0.094	0.020	39.2	0.069
ARAD1K	KAUST	1.391	0.145	19.4	0.408	1.202	0.127	20.6	0.412
		HSCNN+[Shi et al. 2018]							
Trained on	Validated on	MRAE↓	RMSE↓	PSNR↑	SAM↓				
CAVE	CAVE	0.328	0.067	25.4	0.222				
ARAD1K	CAVE	2.522	0.098	21.1	0.419				
ICVL	ICVL	0.223	0.042	28.9	0.029				
ARAD1K	ICVL	0.528	0.074	23.3	0.117				
KAUST	KAUST	2.093	0.192	19.5	0.075				
ARAD1K	KAUST	1.281	0.135	19.9	0.351				

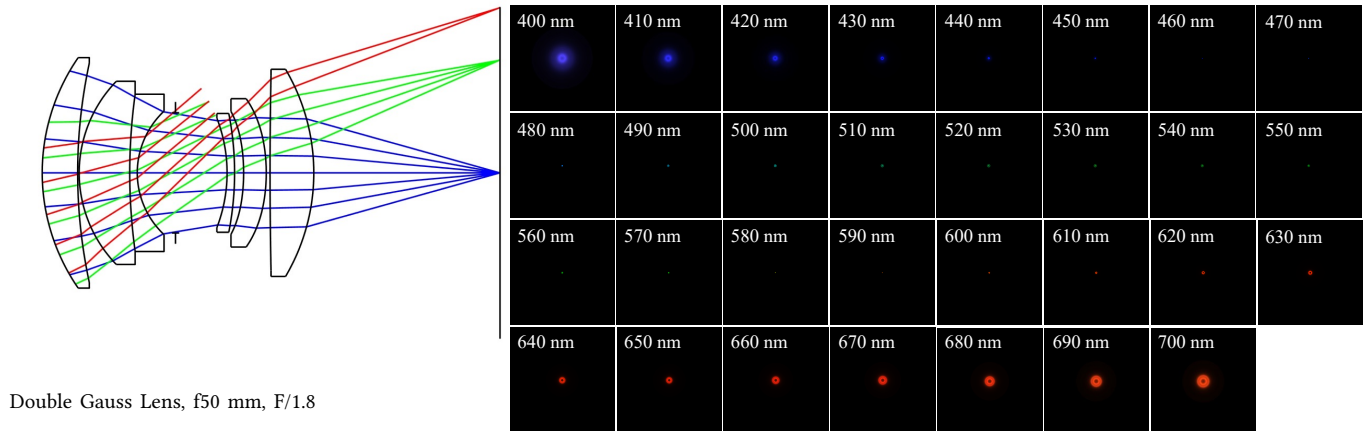


Fig. S1. Double Gauss lens layout (left) and its aberrated spectral PSFs (right). Lens data is obtained from [Ichimura 2021] (Numerical Example 2). Spectral PSFs are modeled in optical design software ZEMAX and rendered in color for the Basler ace 2 camera (model A2a5320-23ucBAS) sensor. Clear chromatic aberrations can be observed throughout the spectral range.

all the networks on the CAVE [Yasuma et al. 2010], ICVL [Arad and Ben-Shahar 2016], and KAUST [Li et al. 2021] datasets. All the results consistently support our conclusion that existing methods cannot distinguish metamers, regardless of the network architectures and datasets.

## 6 RESULTS OF THE ABERRATION ADVANTAGE FOR OTHER NETWORKS AND OTHER DATASETS

In Fig. 4 of the main paper, we demonstrate that it is beneficial to incorporate the realistic chromatic aberrations of the optical system into the training pipeline, such that the spectral accuracy can be improved. To prove that this phenomenon is regardless of the network architectures, we perform the same experiment for the other candidate networks on the ARAD1K dataset. The results are shown in Supplemental Fig. S4 and Fig. S5.

We also demonstrate that the aberration advantage applies to other datasets. Since the MST++ network performs consistently among the top performing architectures, we conduct the same experiments with this network on the CAVE, ICVL, and KAUST datasets. The results are shown in Supplemental Fig. S6. All the results clearly support our conclusion that the chromatic aberrations encode spectral information into the RGB images for the networks to effectively learn the embedded spectra.

## REFERENCES

- Boaz Arad and Ohad Ben-Shahar. 2016. Sparse recovery of hyperspectral signal from natural RGB images. In *Eur. Conf. Comput. Vis.* Springer, 19–34.
- Boaz Arad, Radu Timofte, Rony Yahel, Nimrod Morag, Amir Bernat, Yuanhao Cai, Jing Lin, Zudi Lin, Haoqian Wang, Yulun Zhang, et al. 2022. NTIRE 2022 spectral recovery challenge and data set. In *IEEE Conf. Comput. Vis. Pattern Recog. Worksh.* 863–881.
- Yuanhao Cai, Jing Lin, Xiaowan Hu, Haoqian Wang, Xin Yuan, Yulun Zhang, Radu Timofte, and Luc Van Gool. 2022a. Mask-guided spectral-wise transformer for efficient hyperspectral image reconstruction. In *IEEE Conf. Comput. Vis. Pattern Recog.* 17502–17511.
- Yuanhao Cai, Jing Lin, Zudi Lin, Haoqian Wang, Yulun Zhang, Hanspeter Pfister, Radu Timofte, and Luc Van Gool. 2022b. MST++: Multi-stage spectral-wise transformer for efficient spectral reconstruction. In *IEEE Conf. Comput. Vis. Pattern Recog. Worksh.* 745–755.

- Liangyu Chen, Xin Lu, Jie Zhang, Xiaojie Chu, and Chengpeng Chen. 2021. HINet: Half instance normalization network for image restoration. In *IEEE Conf. Comput. Vis. Pattern Recog.* 182–192.
- Robert Edward Fischer, Biljana Tadic-Galeb, Paul R Yoder, Ranko Galeb, Bernard C Kress, Stephen C McClain, Tom Baur, Richard Plympton, Bob Wiederhold, and Bob Grant Alastair J. 2000. *Optical system design*. Vol. 599. Citeseer.
- Xiaowan Hu, Yuanhao Cai, Jing Lin, Haoqian Wang, Xin Yuan, Yulun Zhang, Radu Timofte, and Luc Van Gool. 2022. HDNet: High-resolution dual-domain learning for spectral compressive imaging. In *IEEE Conf. Comput. Vis. Pattern Recog.* 17542–17551.
- Junya Ichimura. 2021. Optical system and image pickup apparatus having the same. US Patent App. 17/174,832.
- Jiaojiao Li, Chaoxiang Wu, Rui Song, Yunsong Li, and Fei Liu. 2020. Adaptive weighted attention network with camera spectral sensitivity prior for spectral reconstruction from RGB images. In *IEEE Conf. Comput. Vis. Pattern Recog. Worksh.* 462–463.
- Yuqi Li, Qiang Fu, and Wolfgang Heidrich. 2021. Multispectral illumination estimation using deep unrolling network. In *Int. Conf. Comput. Vis.* 2672–2681.
- Bee Lim, Sanghyun Son, Heewon Kim, Seungjun Nah, and Kyoung Mu Lee. 2017. Enhanced deep residual networks for single image super-resolution. In *IEEE Conf. Comput. Vis. Pattern Recog. Worksh.* 136–144.
- Zhan Shi, Chang Chen, Zhiwei Xiong, Dong Liu, and Feng Wu. 2018. HSCNN+: Advanced CNN-based hyperspectral recovery from RGB images. In *IEEE Conf. Comput. Vis. Pattern Recog. Worksh.* 939–947.
- Warren J Smith. 2008. *Modern optical engineering: the design of optical systems*. McGraw-Hill Education.
- Fumihito Yasuma, Tomoo Mitsunaga, Daisuke Iso, and Shree K Nayar. 2010. Generalized assorted pixel camera: postcapture control of resolution, dynamic range, and spectrum. *IEEE Trans. Image Process.* 19, 9 (2010), 2241–2253.
- Syed Waqas Zamir, Aditya Arora, Salman Khan, Munawar Hayat, Fahad Shahbaz Khan, and Ming-Hsuan Yang. 2022. Restormer: Efficient transformer for high-resolution image restoration. In *IEEE Conf. Comput. Vis. Pattern Recog.* 5728–5739.
- Syed Waqas Zamir, Aditya Arora, Salman Khan, Munawar Hayat, Fahad Shahbaz Khan, Ming-Hsuan Yang, and Ling Shao. 2020. Learning enriched features for real image restoration and enhancement. In *Eur. Conf. Comput. Vis.* Springer, 492–511.
- Syed Waqas Zamir, Aditya Arora, Salman Khan, Munawar Hayat, Fahad Shahbaz Khan, Ming-Hsuan Yang, and Ling Shao. 2021. Multi-stage progressive image restoration. In *IEEE Conf. Comput. Vis. Pattern Recog.* 14821–14831.
- Yuzhi Zhao, Lai-Man Po, Qiong Yan, Wei Liu, and Tingyu Lin. 2020. Hierarchical regression network for spectral reconstruction from RGB images. In *IEEE Conf. Comput. Vis. Pattern Recog. Worksh.* 422–423.

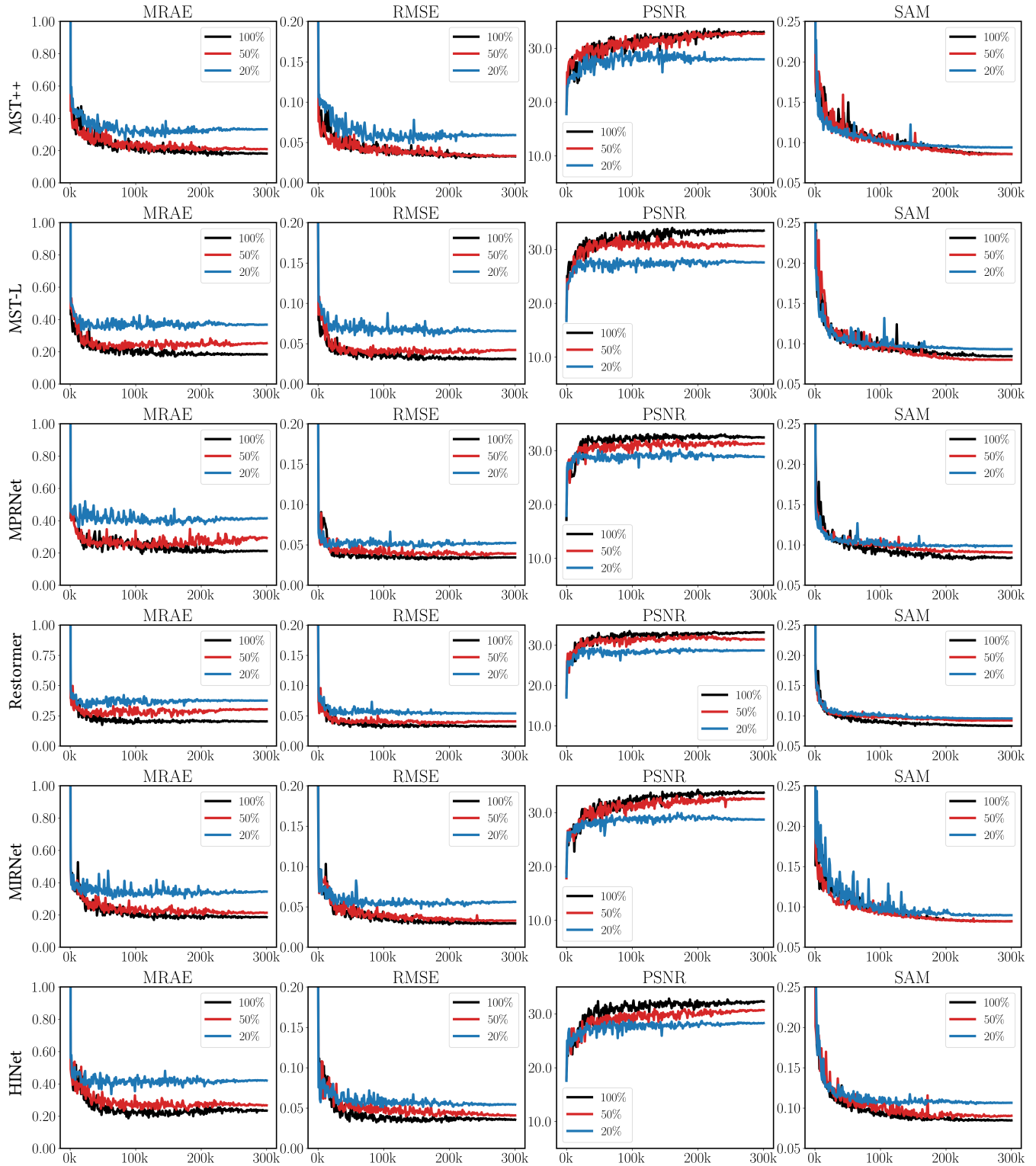


Fig. S2. Validation performance on MRAE, RMSE, PSNR, and SAM for MST++ [Cai et al. 2022b], MST-L [Cai et al. 2022a], MPRNet[Zamir et al. 2021], Restormer[Zamir et al. 2022], MIRNet[Zamir et al. 2020], and HINet[Chen et al. 2021] with 100%, 50%, and 20% of the original training data on the ARAD1K dataset.

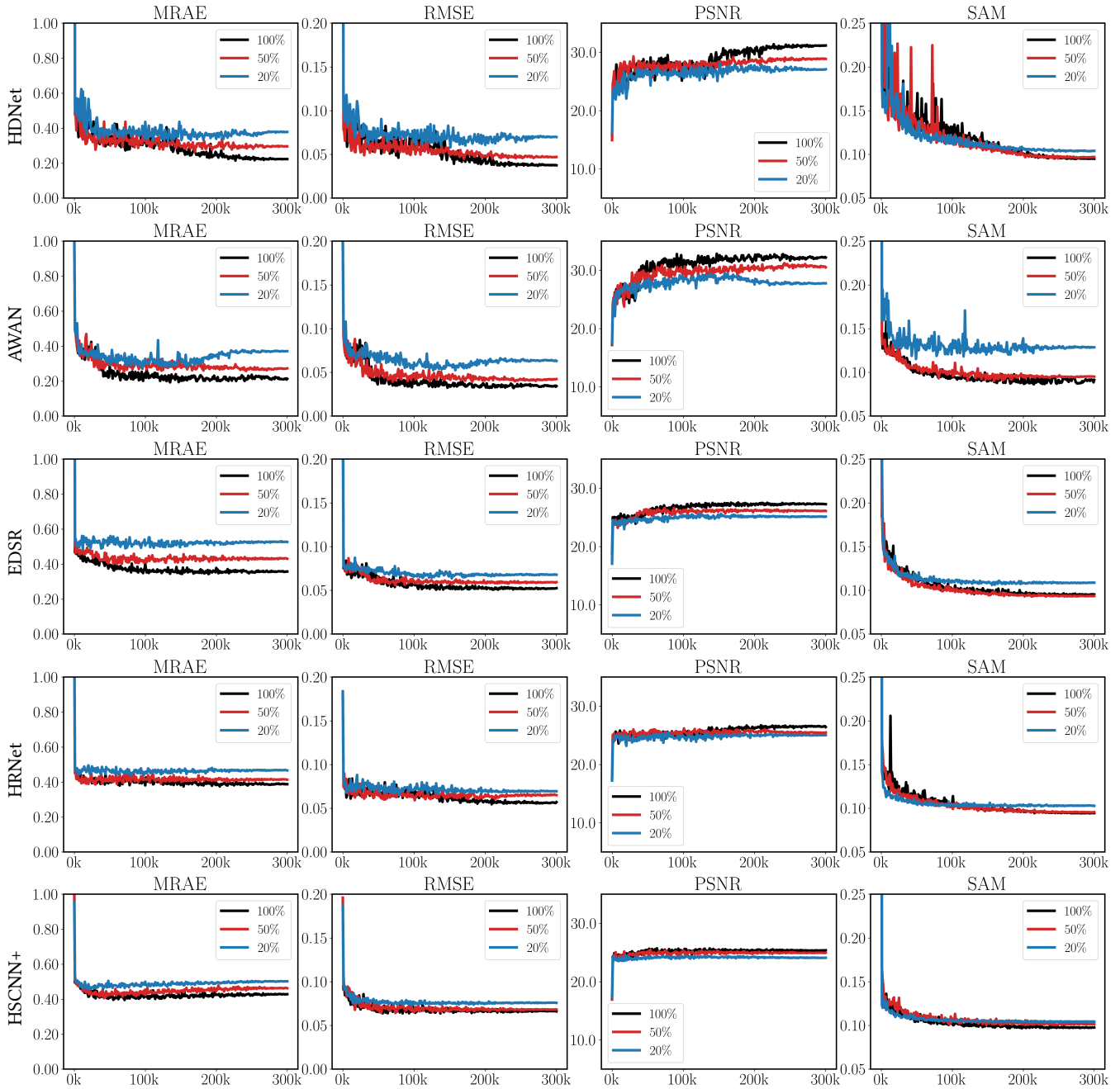


Fig. S3. Validation performance on MRAE, RMSE, PSNR, and SAM for HDNet[[Hu et al. 2022](#)], AWAN[[Li et al. 2020](#)], EDSR[[Lim et al. 2017](#)], HRNet[[Zhao et al. 2020](#)], and HSCNN+[[Shi et al. 2018](#)] with 100%, 50%, and 20% of the original training data on the ARAD1K dataset.

Table S.III. Training with metamers on the CAVE, ICVL, and KAUST datasets. Part I: MST++, MST-L, MPRNet, Restormer, MIRNet, and HINet.

Dataset	Metamer	MST++[Cai et al. 2022b]				MST-L[Cai et al. 2022a]			
		MRAE↓	RMSE↓	PSNR↑	SAM↓	MRAE↓	RMSE↓	PSNR↑	SAM↓
CAVE[Yasuma et al. 2010]	no	1.014	0.038	29.9	0.192	0.932	0.057	26.1	0.195
	fixed	38.26	0.053	29.6	0.229	66.470	0.062	27.6	0.295
	on-the-fly	226.0	0.078	25.2	0.451	286.557	0.085	24.7	0.504
ICVL[Arad and Ben-Shahar 2016]	no	0.067	0.016	40.1	0.027	0.067	0.015	39.8	0.025
	fixed	1.454	0.041	34.8	0.229	2.080	0.040	34.5	0.28
	on-the-fly	2.615	0.087	24.3	0.268	3.281	0.087	23.7	0.261
KAUST[Li et al. 2021]	no	0.082	0.016	43.2	0.076	0.097	0.017	42.0	0.074
	fixed	2.033	0.022	39.0	0.217	1.920	0.022	38.8	0.219
	on-the-fly	1.874	0.032	33.7	0.245	4.235	0.023	39.8	0.236
Dataset	Metamer	MPRNet[Zamir et al. 2021]				Restormer[Zamir et al. 2022]			
		MRAE↓	RMSE↓	PSNR↑	SAM↓	MRAE↓	RMSE↓	PSNR↑	SAM↓
CAVE[Yasuma et al. 2010]	no	1.110	0.041	30.3	0.177	0.987	0.040	29.5	0.175
	fixed	34.272	0.046	32.3	0.209	93.697	0.047	34.7	0.276
	on-the-fly	355.958	0.112	22.8	0.626	379.277	0.093	25.7	0.501
ICVL[Arad and Ben-Shahar 2016]	no	0.084	0.019	38.2	0.025	0.083	0.020	38.2	0.026
	fixed	1.693	0.041	33.4	0.228	1.730	0.040	34.7	0.228
	on-the-fly	2.584	0.094	22.9	0.259	2.254	0.099	22.7	0.272
KAUST[Li et al. 2021]	no	0.071	0.013	43.6	0.066	0.063	0.013	44.6	0.063
	fixed	2.668	0.024	35.7	0.216	2.077	0.020	40.3	0.213
	on-the-fly	2.431	0.037	32.2	0.251	2.623	0.032	34.1	0.281
Dataset	Metamer	MIRNet[Zamir et al. 2020]				HINet[Chen et al. 2021]			
		MRAE↓	RMSE↓	PSNR↑	SAM↓	MRAE↓	RMSE↓	PSNR↑	SAM↓
CAVE[Yasuma et al. 2010]	no	1.167	0.035	31.5	0.190	1.064	0.050	27.3	0.196
	fixed	29.483	0.044	31.7	0.212	55.259	0.056	29.2	0.223
	on-the-fly	131.464	0.083	25.0	0.405	141.691	0.072	27.5	0.362
ICVL[Arad and Ben-Shahar 2016]	no	0.070	0.015	39.7	0.025	0.071	0.017	38.9	0.027
	fixed	3.794	0.038	35.0	0.227	2.445	0.041	34.8	0.228
	on-the-fly	2.895	0.095	23.0	0.265	3.600	0.092	23.4	0.271
KAUST[Li et al. 2021]	no	0.078	0.015	42.2	0.069	0.097	0.017	41.9	0.080
	fixed	2.072	0.021	38.7	0.216	2.481	0.023	37.5	0.218
	on-the-fly	2.312	0.037	33.1	0.257	4.323	0.023	38.9	0.229

Table S.IV. Training with metamers on the CAVE, ICVL, and KAUST datasets. Part II: HDNet, AWAN, MIRNet, HINet, and HSCNN+.

		HDNet[ <a href="#">Hu et al. 2022</a> ]				AWAN[ <a href="#">Li et al. 2020</a> ]			
Dataset	Metamer	MRAE↓	RMSE↓	PSNR↑	SAM↓	MRAE↓	RMSE↓	PSNR↑	SAM↓
CAVE[ <a href="#">Yasuma et al. 2010</a> ]	no	1.071	0.043	29.4	0.197	1.045	0.069	24.7	0.208
	fixed	56.996	0.071	26.8	0.298	88.236	0.072	28.8	0.291
	on-the-fly	78.524	0.093	23.8	0.274	259.101	0.079	26.7	0.366
ICVL[ <a href="#">Arad and Ben-Shahar 2016</a> ]	no	0.076	0.019	37.2	0.027	0.100	0.020	37.9	0.028
	fixed	2.786	0.039	34.0	0.226	3.034	0.040	34.3	0.230
	on-the-fly	2.891	0.091	23.3	0.259	2.707	0.094	22.8	0.280
KAUST[ <a href="#">Li et al. 2021</a> ]	no	0.085	0.017	40.8	0.082	0.101	0.017	39.6	0.105
	fixed	2.891	0.022	37.9	0.217	2.152	0.021	38.3	0.221
	on-the-fly	3.789	0.023	38.9	0.233	3.855	0.024	38.2	0.233
		EDSR[ <a href="#">Lim et al. 2017</a> ]				HRNet[ <a href="#">Zhao et al. 2020</a> ]			
Dataset	Metamer	MRAE↓	RMSE↓	PSNR↑	SAM↓	MRAE↓	RMSE↓	PSNR↑	SAM↓
CAVE[ <a href="#">Yasuma et al. 2010</a> ]	no	1.207	0.057	26.3	0.202	1.087	0.056	26.6	0.198
	fixed	54.125	0.066	27.0	0.292	106.082	0.065	27.3	0.310
	on-the-fly	199.916	0.106	21.2	0.371	151.295	0.100	21.8	0.356
ICVL[ <a href="#">Arad and Ben-Shahar 2016</a> ]	no	0.112	0.029	32.9	0.028	0.106	0.027	33.3	0.029
	fixed	2.275	0.045	30.5	0.227	2.182	0.045	30.8	0.228
	on-the-fly	2.721	0.093	23.0	0.262	2.703	0.083	24.0	0.244
KAUST[ <a href="#">Li et al. 2021</a> ]	no	0.260	0.044	30.5	0.085	0.097	0.021	37.8	0.070
	fixed	2.002	0.033	32.2	0.218	2.819	0.024	37.5	0.218
	on-the-fly	3.883	0.025	36.1	0.221	3.373	0.026	36.9	0.223
		HSCNN+[ <a href="#">Shi et al. 2018</a> ]							
Dataset	Metamer	MRAE↓	RMSE↓	PSNR↑	SAM↓				
CAVE[ <a href="#">Yasuma et al. 2010</a> ]	no	1.027	0.065	25.3	0.229				
	fixed	55.611	0.076	25.1	0.313				
	on-the-fly	154.416	0.104	21.8	0.353				
ICVL[ <a href="#">Arad and Ben-Shahar 2016</a> ]	no	0.226	0.043	28.6	0.030				
	fixed	1.908	0.052	28.1	0.229				
	on-the-fly	1.627	0.102	21.9	0.253				
KAUST[ <a href="#">Li et al. 2021</a> ]	no	1.832	0.171	19.9	0.077				
	fixed	6.240	0.166	20.6	0.217				
	on-the-fly	2.669	0.057	25.9	0.222				

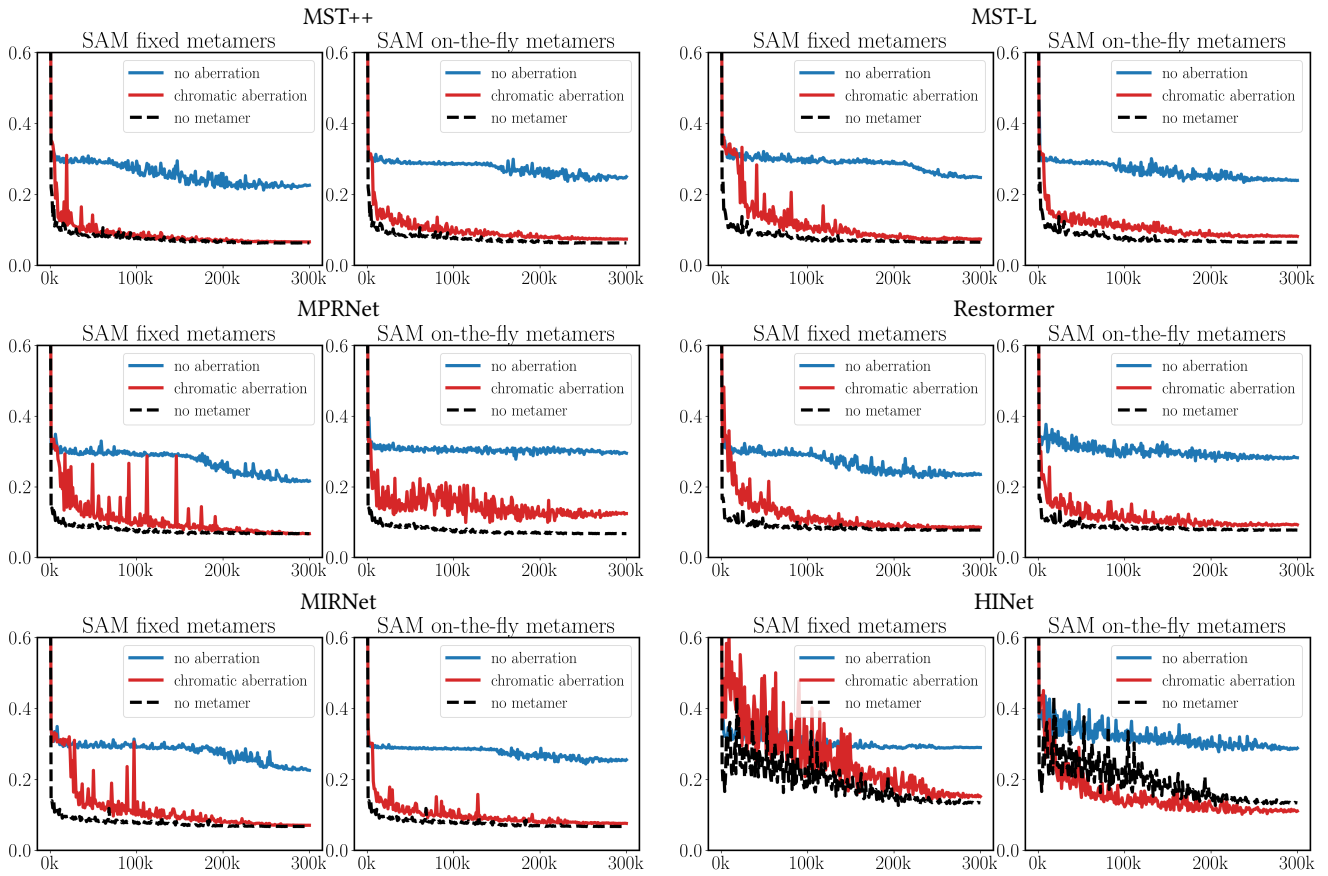


Fig. S4. Chromatic aberrations improve spectral accuracy for MST++, MST-L, MPRNet, Restormer, MIRNet, and HINet. In each group, left: fixed metamers, and right: on-the-fly metamers.

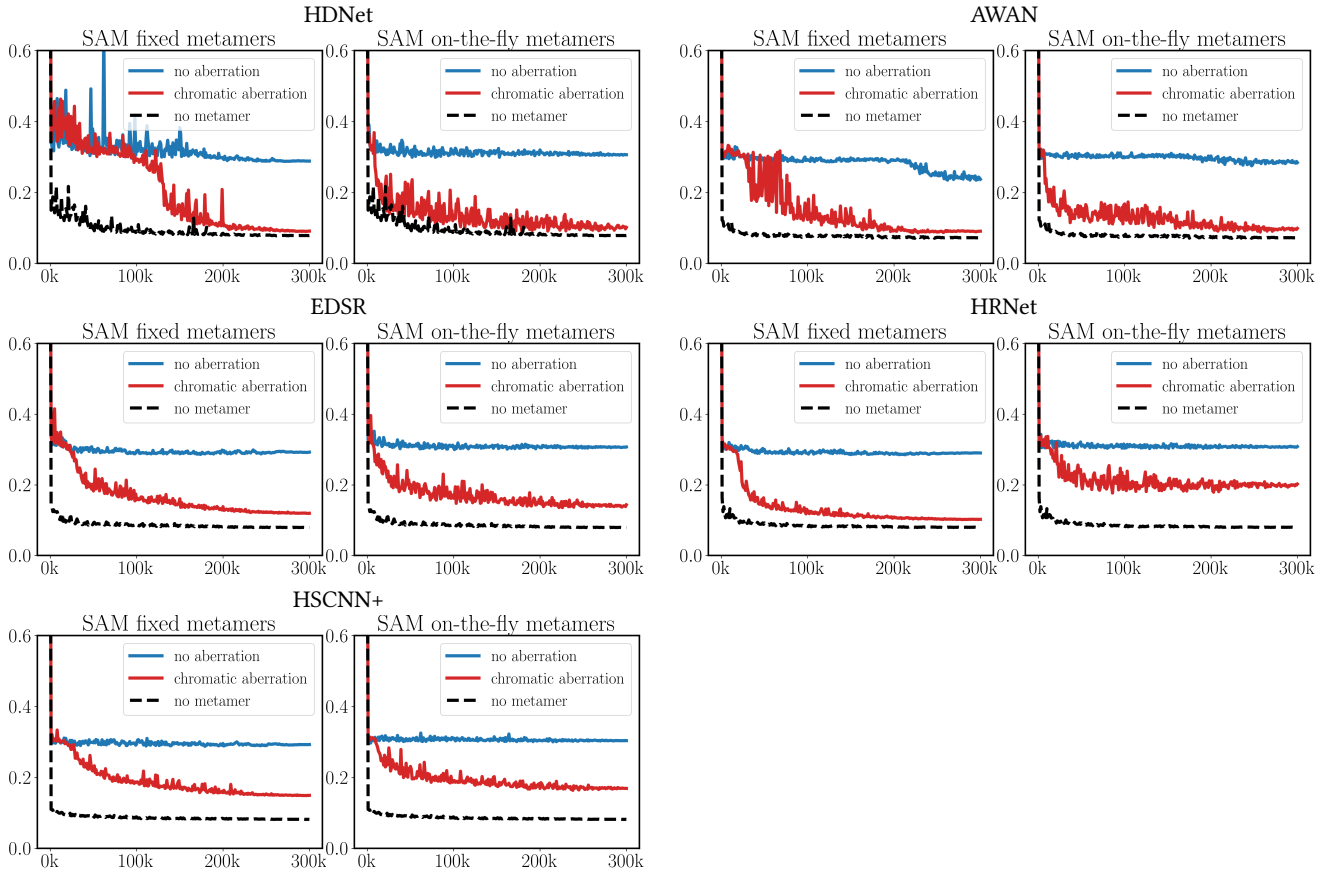


Fig. S5. The aberration advantage results for HDNet, AWAN, EDSR, HRNet, and HSCNN+ on ARAD1K. In each group, left is for fixed metamers, and right is for on-the-fly metamers.

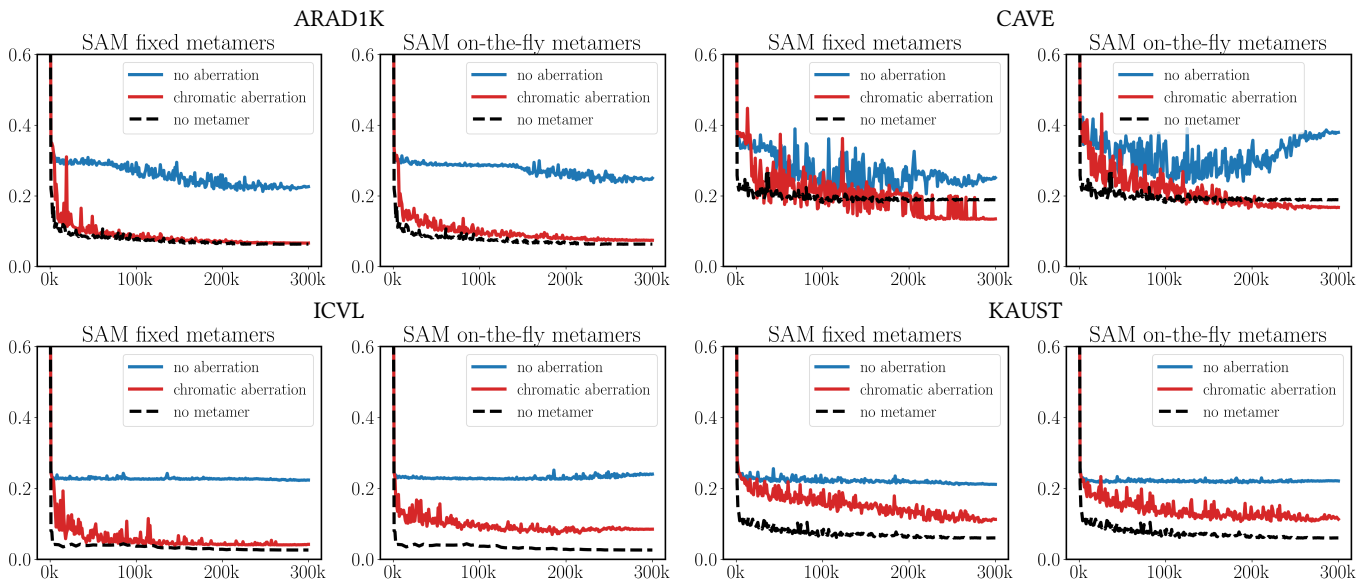


Fig. S6. The aberration advantage results for MST++ on all datasets. In each group, left is for fixed metamers, and right is for on-the-fly metamers.